Lens Characterization for Multifocus Microscopy Applications

By: Brandon Lynch

University of California, Santa Cruz

Advisor: Sara Abrahamsson

March 2019

Abstract

In this study, a lens characterization system was constructed in order to compare the light efficiency and aberration robustness of an achromatic doublet lens to a camera lens in order to determine their effectiveness as the secondary relay lens in a Multifocus Microscopy (MFM) imaging system. To do this, a custom epifluorescence microscope was constructed with a 50/50 beamsplitter to allow for Point Spread Functions to be recorded on two different cameras using the two different lenses simultaneously. These Point Spread Functions allowed for aberration to be observed and intensity profile plots at the in-focus plane to be fit to distributions to calculate experimental resolution and light efficiency. After characterizing the aligned system, the camera lens and achromatic doublet lens were misaligned laterally by the same amount before recording more PSFs allowing for characterization of the imperfections in the outer regions of the lenses. After completing this project, I concluded that while the achromatic doublet lens did appear to be more light efficient than the camera lens, misalignment of 10mm laterally caused the light efficiency of the achromatic doublet to approach that of the camera lens. Also at 10mm misalignment, there is evidence that the achromatic doublet arm's resolution began to worsen. These findings imply that the outer local regions of the camera lens are more consistent for maintaining light efficiency and resolution when compared to the center region than the achromatic doublet's.

Acknowledgements

I would like to first thank my advisor Sara Abrahamsson for the advice, materials, and support that I required to complete this project. Next, I would like to thank the members of the Saralab, Eduardo Hirata, Juliana Hernandez, and Gustav Pettersson for their support. I would also like to thank Robert Shelansky from the Boeger lab for advice regarding sample preparation techniques. Also, I would like to thank Joe Cox from the Machine shop for letting me borrow his height probe. Finally, I want to thank my parents for their continuous support through my undergraduate career.

Table of Contents

1 Problem Statement

My goal is to build a lens characterization system to determine if the achromatic doublet lens, which serves as the secondary relay lens in a Multifocus Microscopy (MFM) system, could be replaced with a camera lens in order to improve MFM system performance[2]. MFM has been made possible by utilizing diffractive fourier optics to multiplex light from different focal planes on a single camera sensor to produce an instantaneous 3D image from the resulting 2D focal stack. Since MFM image acquisition speed is limited by the readout speed of a single camera, this method provides the unique opportunity to image fast biological events, such as neuron activity, at higher speeds than alternative 3D imaging methods[2]. When designing MFM systems, there is a strong desire to prevent aberration in the 2D focal stack of images. Any reduction in system aberration will directly translate to better system resolution which, in the case of super-resolution imaging techniques, is significant. In addition to reducing aberration, producing high contrast and low noise images of small singular biomolecules requires maximization of photon collection efficiency. It is therefore important to compare the properties of these two large lenses under unique MFM conditions before implementing them in an MFM system[2].

To evaluate an imaging system's performance, Point Spread Functions (PSFs) can be recorded by imaging sub-resolution point sources. This is an appealing way to characterize optical systems like the one I plan to build since characterization by this method does not require the specific components involved in image formation to be

known. Since I will not know what optical elements exist inside of the camera lens, I will need to treat the lens like a "black box" and characterize it as a single unknown optical component.

To compare the two lenses, I will build and align an optical system that can record two PSFs simultaneously. General alignment procedures can be found in Sara Abrahamsson et al. (2015) and details regarding this specific system's alignment can be found in appendix #1 of this paper[2]. To record PSFs with my system, I plan to image sub-resolution fluorescent microspheres using the software μmanager to sweep the microspheres through focus to produce a focal stack of 3D PSF data as a function of defocus. After recording PSFs, characterization will be done by fitting Gaussian distributions to the intensity profiles of the PSFs at the in-focus plane. This will allow calculations to be made for resolution and maximum intensity in the PSF data. If an increase in the resolution calculation is observed, I will then attempt to characterize the aberrations that might be causing the worsening in resolution by looking at the 3D PSF data. Light efficiency will be estimated by comparing the maximum pixel values between the PSFs. In addition to maximum pixel values, I will also look at the integrated density values under the surface plot curve at the in-focus plane. The benefit to this measurement is that it is a sum of all of the bead's light that is focused on the camera sensor. Since the only difference between the optical paths that will form the two images is the lenses that I am comparing, any difference in light efficiency or increase in resolution will be a direct result of imaging with the lenses of interest.

After successfully recording PSFs and modeling them using a well aligned system, PSFs will be recorded when the lenses and cameras are misaligned by translating the lenses perpendicular to the beam path an equal distance. After investigating the effects on aberration and resolution when the lenses are misaligned, I will be able to make inferences regarding lens robustness to aberration when imaging with the outer local regions of the lens. I will also look at the maximum intensity values and the integrated

density values to compare the light efficiency of the lenses as a function of lateral misalignment. This is a useful property for these lenses to have since MFM systems require the outer regions of the glass to refocus the non-zero diffraction orders of multiplexed light on the camera sensor.

2 Background

2.1 Introduction to Optical System Design

The history of optical lenses spans back as far as the Old Kingdom Period (2600 BC) in ancient Egypt. The Egyptians from this time period often constructed the eyes of statues with highly polished convex quartz crystals creating the illusion that the eyes of the statues were tracking observers as they moved around the room[4]. While certainly an advanced technology for the time period, explanations regarding lens refraction and image formation were largely inaccurate until 1621 AD when Dutch mathematician and astronomer Willebrord Snell managed to correctly describe refraction. Snell was able to describe the propagation of light as it moves through various medium which eventually led to the development of the famous Snell's law equation $n_1 sin(\theta_1) = n_2 sin(\theta_2)$ where n is refractive index and θ is incident angle. Incident angle is the angle between the light's propagation direction when it encounters the new medium and the axis perpendicular to the surface of the medium. This advancement was fundamental to the development of early optical imaging theory and spawned the birth of first order geometric optics. Today, it is typical for imaging systems to be designed using geometric optics to determine image size and location. While these calculations provide a starting point for system design, they assume ideal "thin lens" properties which ignores the effects that real spherical lenses have on image formation.

Before discussing the non-ideality of spherical lenses, it is important to discuss how

images are formed with ideal lenses. Figure 2.1 depicts an ideal converging lens imaging an object in the form of an arrow. In this Figure, the incoming light that is propagating parallel to the optical axis is focused to a point a distance f away from the lens. This distance f is called the focal length of the lens. Parallel beams of light are commonly referred to as collimated and the convergence of this beam to a focal point behind the lens, defines the lens as a positive, or converging. From Figure 2.1, we can draw the thin lens equation which relates the distance between object, image, and focal length. The thin lens equation is typically written as $\frac{1}{f} = \frac{1}{di} + \frac{1}{do}$ where f is focal length, do is distance from object to lens, and di is distance from lens to image. It is also important to note the magnification of this system: $M = \frac{-Hi}{Ho} = \frac{d_i}{d_o}$ where H_o is object size and Hi is image size. The negative value in this case for the magnification is a sign convention and is defined as negative because the image of the object is inverted.

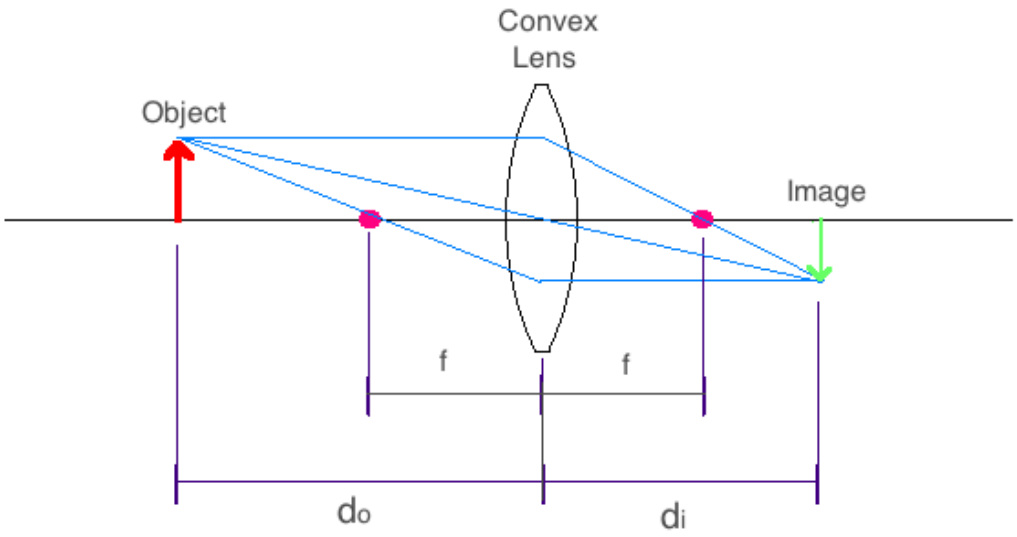

Figure 2.1: Taken directly from the Converging Geometric Optics: convex lens page on the Rutgers School of Arts and Sciences website `http://www.physics.rutgers.edu/analyze/wiki/lens_equation.html`
This Figure shows a ray tracing of an object being imaged by an ideal convex lens. The thin lens equation relating the distances di, do and f is $\frac{1}{f} = \frac{1}{di} + \frac{1}{do}$

Now if an additional lens is placed in the system, we might end up with something that looks like the relay lenses depicted in Figure 2.2. Using geometric optics, this system can be described with two copies of the thin lens equation. The relay lens design is particularly interesting because we are now provided with the opportunity to simplify the already simple thin lens equations by positioning the leftmost image plane at the focal length of the first lens. This results in the secondary image plane forming at a focal length behind the second lens. Also called a 4f system, the magnification from the object plane to the image plane in Figure 2.2 is $M = -\frac{F2}{F1}$ where $F2$ and $F1$ are focal length.

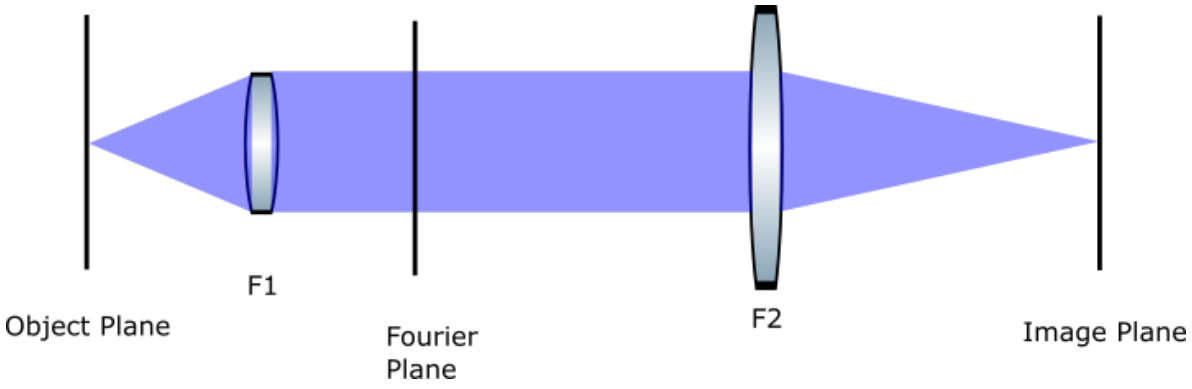

Figure 2.2: This Figure depicts a relay lens design where the object is being magnified by $M = -\frac{F2}{F1}$. This is because the object's distance from the first lens is set equal to $F1$.

2.2 Introduction to Fourier Optics

The 4f system is commonly implemented when building fourier optic systems because it allows for a fourier plane to be generated at a distance $F1$ behind the first lens as long as the object is placed a focal length in front of lens $F1$. Fourier optics is more intuitive to understand when visualizing light propagation as a sum of planar wavefronts. This idea is illustrated in Figure 2.3, where if we assume that the wavefronts are propagating right to left from ip a distance f from a convex lens, the light is collimated and refracted into "flat" non-diverging wavefronts. Similarly, if we assume the light is propagating left to right in Figure 2.3, the flat wavefronts are being bent by the lens into focus at point ip.

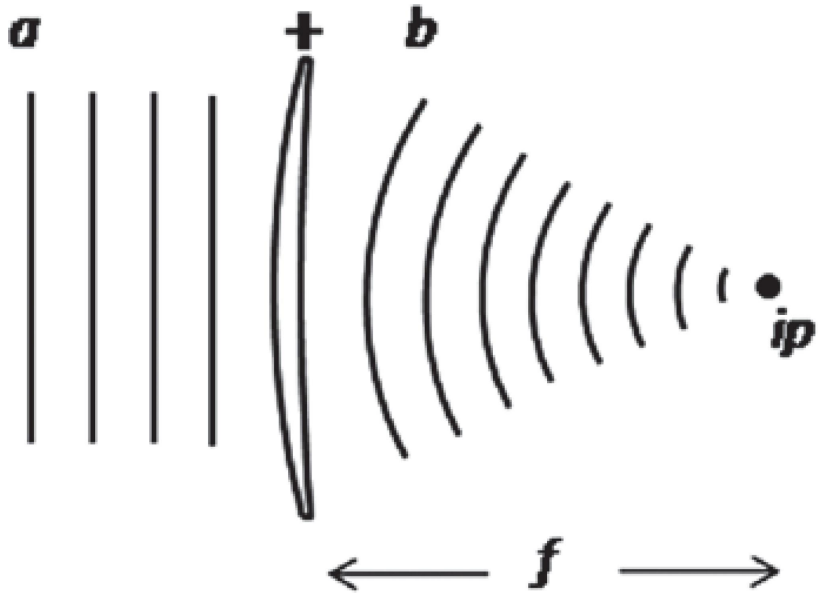

Figure 2.3: Taken directly from visual optics under the wavefront perspective Sidney Júlio Faria-E-Sousa (2014) http://www.scielo.br/scielo.php?script=sci_arttext&pid=S0004-27492014000400267} This Figure depicts the propagation of a spherical wavefront being converged by a convex lens into a flat collimated wavefront. This serves as a visual representation of how ray diagrams can instead be thought of as a sum of planar wavefronts

The fourier plane that forms one focal length behind lens $F1$ in the 4f system depicted in Figure 2.2 is significant because light at the fourier plane contains the spatial frequency information of its spatial equivalent at the image plane. In other words, the light distribution at this fourier plane is the fourier transform of the light at the primary image plane[8]. This fundamental property of lenses provides the opportunity to induce phase shifts and multiplex different focal planes of light using diffraction[9]. After splitting the light into diffraction orders via a carefully designed Multifocus Diffraction Grating (MFG) and flattening the wavefronts, the light can then be refocused by a secondary relay lens resulting in the array of focus stepped images characteristic of Multifocus Microscopy (MFM) imaging systems[2]. The Multifocus optics described in Abrahamsson et al. (2015) can be seen in Figure 2.4.

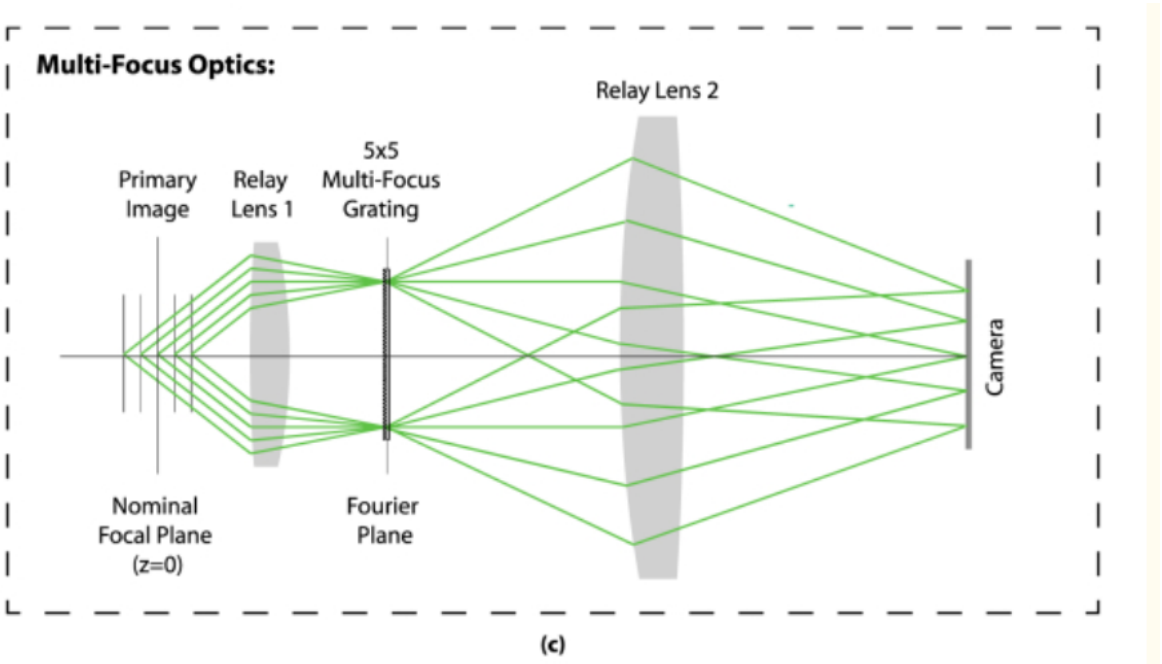

Figure 2.4: This Figure is taken directly from MultiFocus Polarization Microscope (MF-PolScope) for 3D polarization imaging of up to 25 focal planes simultaneously [2].
The Figure depicts the multifocus optics in an MFM system design where a Multifocus Grating(MFG) placed in the fourier plane of the 4f system is splitting the light up via diffraction orders into flat wavefronts corresponding to different focal planes. The diffracted light is then refocused by relay lens 2 into an array of 2D images on the camera sensor.

2.3 Beam Expanders

If instead now we consider the case when the light entering a relay lens system is collimated to begin with, we end up with the Keplerian Beam expander design depicted in Figure 2.5. In this design, the diameter of the collimated beam after F2 should be equal to the laser beam's diameter multiplied by the magnification $\frac{F2}{F1}$ where $F1$ and $F2$ are focal length.

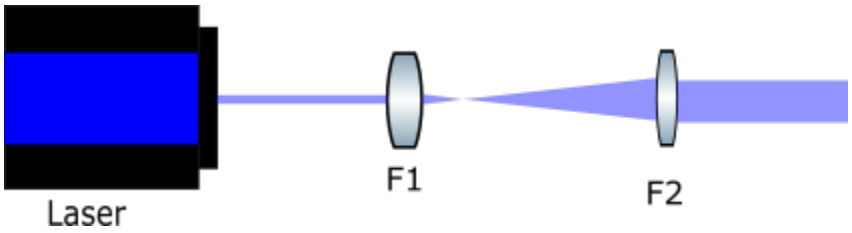

Figure 2.5: This keplerian beam expander design depicts the expansion of a beams diameter by a factor of $M = \frac{F2}{F1}$ where $F2$ and $F1$ are focal lengths. This is a common way to increase the diameter of a collimated beam.

2.4 Wide-field Epifluorescence Microscopy and Multifocus systems

Epifluorescence microscopes are imaging systems that are designed to image fluorescent samples that emit a different wavelength of light than is used for excitation. A dichroic mirror, like the one depicted as DM in Figure 2.6, is typically used to separate the emission and excitation beam paths as it reflects and transmits different wavelengths of light. Separating the emission and excitation light provides the opportunity to image with a high signal-to-noise ratio (STNR), which is essential when imaging small singular fluorescent biomolecules at high-speeds [2]. An epifluorescence microscope is depicted in Figure 2.6.

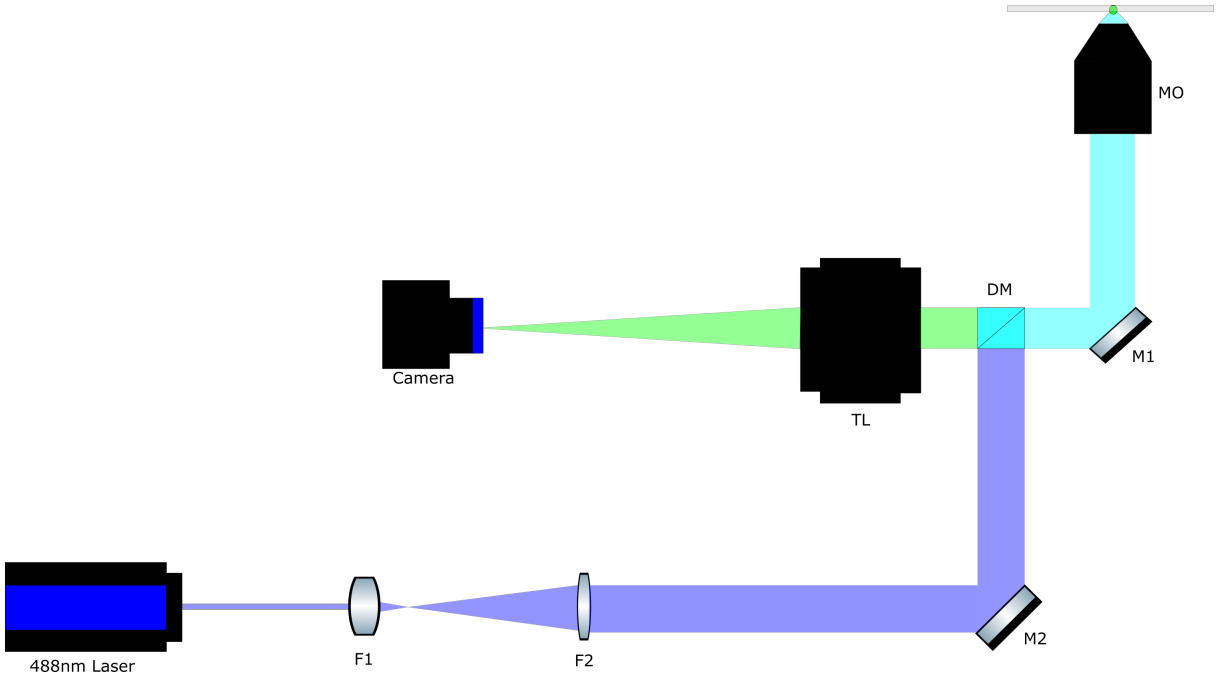

Figure 2.6: This Figure is of an epifluorescent microscope. In this example, MO is the microscope objective, M1 and M2 are mirrors, TL is an tube lens (a series of lenses designed to focus the collimated light from the microscope objective), DM is dichromic mirror that is reflecting illumination wavelength and transmitting the emission wavelength and F1 and F2 are biconvex lenses that form a keplarian beam expander.

In general the main goal in creating effective fluorescence microscopy systems is to create systems that can image with high spatial resolution while maximizing STNR [2]. More recently, it has also become increasingly desirable to design systems that can image biological events at high spatial and temporal resolution in 3 dimensions, since insight into 3D structures can provide the opportunity to learn more about complex cellular networks. In the case of fast 3D cellular networks such as neural networks, three-dimensional organization and communication between neurons is essential to understanding how they function[5]. With the exception of MFM, most 3D imaging methods are too slow to capture fast biological events such as neuron activity[1]. Even with the development of high speed 3D structured illumination (SIM) and lattice light

illumination techniques to increase resolution, there is an inherent spatiotemporal resolution limit to these systems since they are incapable of capturing multiple focal plane images simultaneously. In addition to ambiguous spatiotemporal information, it is possible that the samples can be perturbed due to stage movements when recording images at high speeds[1]. Therefore, MFM has proved to be a desirable option for high speed single molecule resolution 3D imaging of fast biological events where spatiotemporal resolution is essential.

2.5 Introduction to Aberration

While the described MFM system provides a novel way to 3D image at high speeds, aberration and wave phenomena often results in chromatic and monochromatic aberrations that cause deterioration in image quality and worsening of resolution. For this reason, aberration analysis and correction are extremely important steps to building quality MFM imaging systems[1]. Since microscope objectives are designed to focus light that is propagating at a specific distance, also known as the working distance, and the MFM systems relies on imaging focal planes deep in the sample, there are often problems with spherical aberration in the higher diffractive order focal planes. To correct this, Abrahamsson et al. (2013) implemented the MFG so that it induces a phase shift on the light in an equal but opposite way before it is refocused again on a camera sensor via the secondary relay lens[1]. In addition to this phase correction element, a Color Correction Grating (CCG) has been designed to correct for chromatic aberration induced by the diffraction of different wavelengths of light. This wavelength difference can become a problem even at 30nm wavelength differences, meaning even a single type of fluorophore can cause chromatic aberration in MFM images[1]. After taking care to correct expected aberrations in an MFM system, it is important that none of the other optical components are adding unexpected aberration to the array of

2D images. Since the final component in these MFM imaging systems is the secondary relay lens to refocus the diffracted light, the performance of this relay lens is crucial. Traditionally, MFM systems utilize a large 3 inch diameter achromatic doublet lens for this task[1]. Achromatic doublet lenses reduce aberration by utilizing a converging (crown) and diverging (flint) lens to compensate for the different refractive indexes resulting from imaging different wavelengths of light. The relationship between velocity of light and index of refraction can be expressed as $v = \frac{C}{n}$ where v is velocity, C is speed of light, and n is refractive index of the medium the light is passing through. Velocity of light can be expressed as $v = (f)\lambda$ where f is frequency and λ is wavelength, therefore $(f)\lambda = \frac{C}{n}$. This inverse relationship between wavelength and index of refraction results in lower wavelengths of light having a higher index of refraction than higher wavelength light. Since lower wavelength light has higher optical dispersion than higher wavelengths encountering the same medium, a singular spherical lens element would in theory not be able to focus two wavelengths of light at the exact same distance on the optical path. As can be seen in Figure 2.7, this difference in refractive index can be compensated for by focusing light with an achromatic doublet.

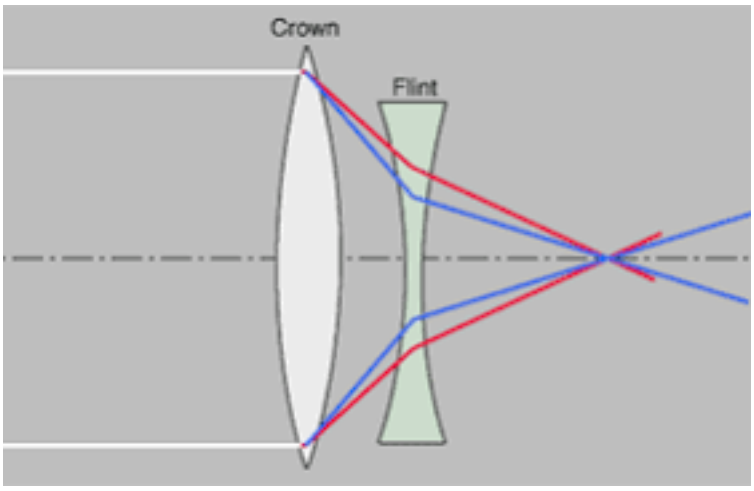

Figure 2.7: Taken directly from hyperphysics website: `http://hyperphysics.phy-astr.gsu.edu/hbase/geoopt/aber2.html`
This Figure depicts an acromatic doublet correcting the chromatic dispersion that arises from the refraction of different wavelengths of light.

While more effective in reducing aberration than a single spherical lens, in reality the achromatic doublet is not a heavily aberration corrected for lens. The desire to design lenses with "thin lens" qualities for all wavelengths of light has pushed lens design towards more complex lens elements with many components. This would be the case with a camera lens and it is possible that when comparing the two lenses, the increase in complexity and components in the camera lens will result in less aberration and distortion in resolved images, however, the increase in lens components might also result in a reduction in the light efficiency of the system. Light efficiency is the amount of light that makes its way from sample to final image plane and its maximization is essential for MFM system design[1].

2.6 Optical System Characterization using the Point Spread Function

Lenses are often characterized based on surface topography using mechanical or optical devices, however, these measurement techniques are typically limited to lower numerical aperture objectives[7]. It is also not possible to characterize complex elements with multiple components via surface topography. Since Point Spread Functions (PSFs) don't require the characterization of individual components, they provide a simple but effective way to characterize complex optical elements as a singular component.

To better understand a system's performance, it is intuitive to look at its response to a known input. In the case of analyzing signals and systems in general, the impulse response of a system can be used to predict output signals for different input signal. This general concept of signal prediction can be translated mathematically to a function called convolution, and this approach to system analysis allows for a system's behavior and transfer function to be modeled while the exact components that make up the system can remain unknown. In the case of imaging systems, this impulse response is referred to as the Point Spread Function(PSF) and can be determined by imaging point sources. After the imaging system's PSF is determined, future image predictions can be made of other known objects. The image generated by an optical system of a known object would therefore appear as the convolution of that object with the system's PSF, resulting in the equation $image = object \circledast PSF$. Based on this equation, the deconvolution of image with the system's PSF would result in the original object. This property has resulted in image deconvolution algorithms to be used to reconstruct more accurate representations of original objects from collected images and the imaging system's PSF [11][3]. This process often employs the conversion of the PSF to frequency domain by taking its fourier transform. This spatial frequency representation of the PSF is called the Optical Transfer function (OTF) and can be used to resolve an image

using the equation $image_f = object_f * OTF$ where $object_f$ and $image_f$ are the spacial frequency representations of object and image respectively[10].

2.7 Sampling and prevention of aliasing

When recording PSFs, special care needs to be taken to ensure it is being sampled correctly both laterally and axially. To avoid aliasing in the lateral plane (xy), the physical size of the camera's pixels rescaled to the field of view (FOV) needs to be 2 times smaller than the objective lens resolution. This allows for the lateral PSFs to remain above the nyquist frequency, which is a standard for ensuring the appropriate sampling frequency of signals. The objective resolution can then be calculated using the Abbe resolution equation $Res = \frac{\lambda}{2NA}$ where is λ is wavelength and NA is the numerical aperture of the objective. The rescaled camera pixel size to the FOV can be found by dividing the camera pixel size by the imaging system's magnification[11].

The axial resolution by Abbe criterion (Rz) required to sample PSFs can be calculated by ensuring that the maximum step axially in recorded PSFs is 2 times smaller than $Rz = \frac{\lambda}{2NA}$[11]. As stated by Cole et al. (2011) the axial step number when acquiring an image can be set such that there will be 21 total focal steps with 10 above and 10 below the in-focus plane[11]. If this amount of steps doesn't suffice in capturing the entire visible PSF, the number of steps should be adjusted so that the image stack spans the entire 3D PSF volume axially. It is also common to sample PSFs using isotropic voxel dimensions. This is a step size that is the camera pixel size divided by the magnification and this sampling allows for similar dimensions for the PSF laterally and axially.

2.8 Optical system resolution

After recording adequately sampled PSFs for a system, analysis can be done to determine if the PSFs display the characteristics of a high quality optical system. In 1873, Ernst Abbe found that the maximum optical resolution for an optical system was physically limited by diffraction [11]. When an optical system's resolution approaches this maximum, it is said to be diffraction-limited. Abbe found this limit to be proportional to wavelength and inversely proportional to the angular distribution of the light, which he expressed as $Res = \frac{\lambda}{2NA}$[12]. In microscopy, this limit is a result of wave driven diffraction through the circular pupil present in the microscope objective. Therefore, a microscope's diffraction-limited PSF would appear as concentric rings representing different diffraction orders with the highest intensity being in the center, at zero-order diffraction. The bright rings result from constructive interference of the diffracted light and the darker rings result from destructive interference[11]. By imaging an object that is smaller than the resolution limit of the objective, these diffraction rings should appear as they appear in Figure 2.8. This image is referred to as the airy disk and it represents the expected 2-dimensional PSF of a diffraction-limited microscopy system with a circular aperture. Figure 2.8 also depicts a profile intensity plot of the 2D PSF. Microscope resolution, via Abbe criterion, is found experimentally by measuring the difference between the half maximum profile intensity plot values at the in-focus plane. This is called the Full width Half Maximum(FWHM). Any aberration in the system should be evident as an increase in the width of this FWHM, so this profile intensity plot is essential when analyzing system aberration and how it affects resolution.

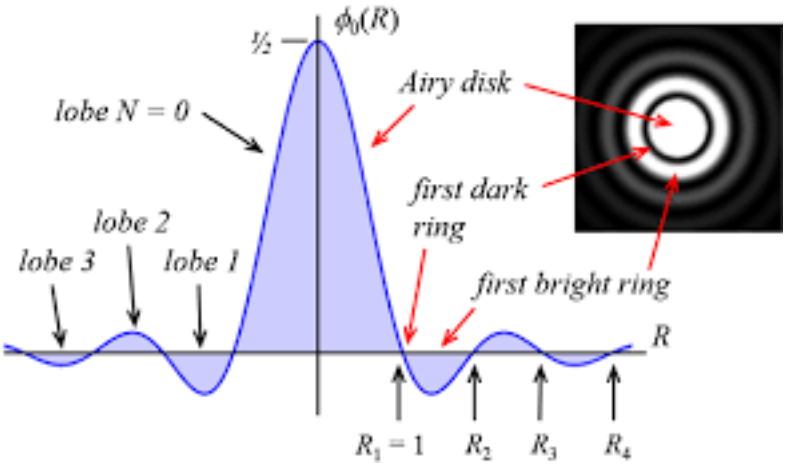

Figure 2.8: Taken directly from The Airy fiber: an optical fiber that guides light diffracted by a circular aperture [6]

This Figure depicts the ideal airy disk pattern as it appears laterally at the in-focus plane as well as the intensity profile of the airy disk pattern at the in-focus plane. It is possible to see the interference patterns in both images due to diffraction through the circular pupil in the objective.

As the sample moves axially, in and out of focus, aberration in the system should be more evident. A 3D PSF from a quality imaging system should appear symmetrical across the zy and zx orthogonal planes. As an example Figure 2.9 depicts a simulation of a series of orthogonal views of PSFs that exhibit varying spherical aberration as a result of index of refraction mismatching between coverslip and mounting media.

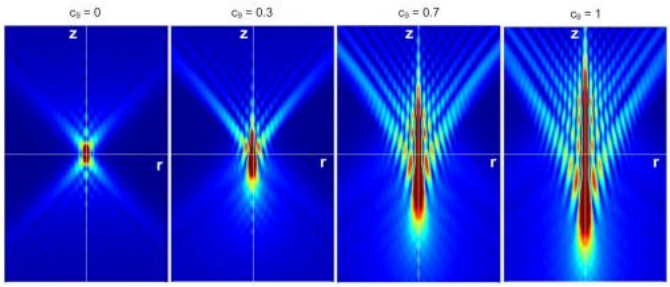

Figure 2.9: This Figure was taken directly from the Institute of Applied Physics website. `https://www.iap.uni-jena.de/Optical+System+Design/Research/KoSimO.html`

The Figure depicts a simulation of varying spherical aberration due to index of refraction mismatching. A PSF from a high quality system will display great symmetry across the orthogonal plane as it does in the leftmost image.

3 Work Done

3.1 Epifluorescence Microscope

Since optics was a new field to me when I began this lens comparison project, I decided it would be a helpful exercise to begin my research by first building a fluorescence microscope with a stage to move the sample axially in and out of focus before moving on to building my final system. This initial design provided the opportunity for me to gain familiarity with both μmanager software and the alignment of more simple systems. This step also allowed for me to observe the aberrations present in the fluorescence microscope before the image is relayed and additional aberrations of interest are expected to be present.

3.1.1 Illumination

My initial fluorescence microscope design involved a Cyan Laser (488nm) which I used to illuminate 100nm yellow-green fluorescent microspheres (emission range 500-580nm). I decided that, for illumination, I would to expand the laser via Keplerian beam expander before launching the beam into the objective. As previously described, the Keplerian beam expander magnifies the beam such that the ratio between output beam diameter and input beam diameter is the same as the ratio of the second lens divided by the first lens. Figure 3.1 was generated after analyzing the Cyan laser with a Thorlabs beam profiler, which is typically used to view the shape of a laser beam's optical

intensity. Using this beam profiler, the laser's original diameter was found to be about 0.8mm. This beam was then expanded using a 25mm biconvex lens (F1) and a 295mm biconvex lens (F2) for an 11.8 magnification. This resulted in the output beam being approximately 9.44mm in diameter before being launched into the microscope objective and focused on the sample. After beam expansion, a 488nm high-pass dichroic mirror, which reflects wavelengths under 488nm and transmits above 488nm, is used to separate the excitation beam from the emission beam.

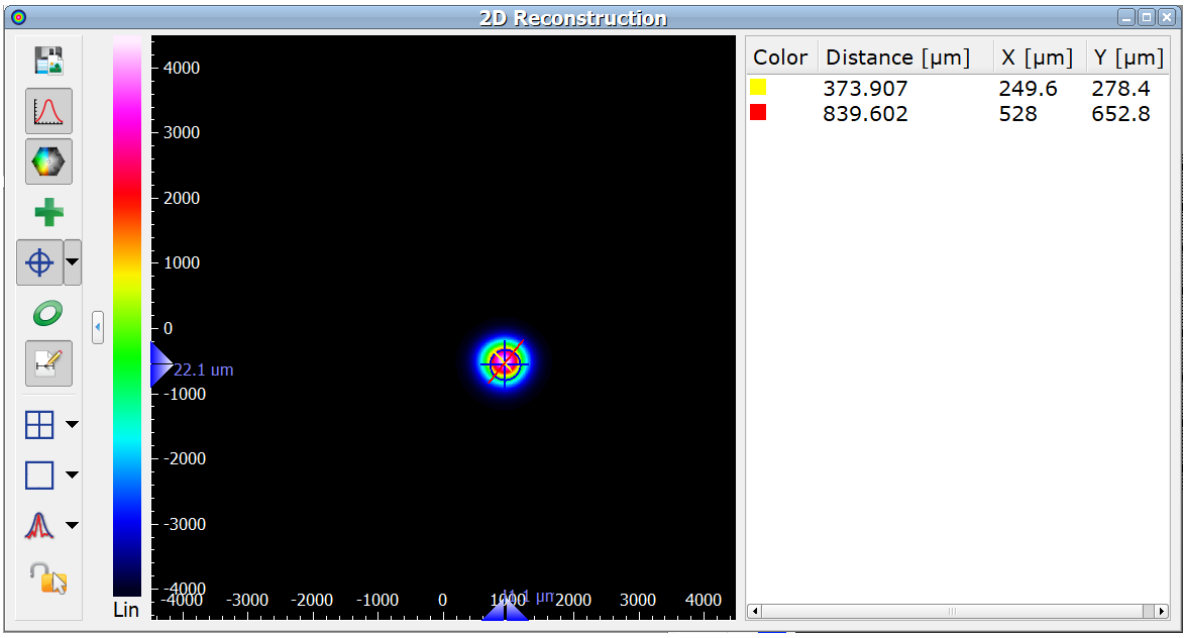

Figure 3.1: Thor Labs beam profiler output. The beam diameter is estimated here to be around .8mm.

3.1.2 Sampling Calculations

After settling on the components of the illumination arm of my system, I began calculations to ensure I would be sampling the PSFs appropriately. Since the UPLSAPO 60X objective I planned to use had a Numerical Aperture (NA) of 1.3, and a 532nm emission wavelength was expected from the yellow-green microsphere beads, the diffraction limited system resolution by abbe criterion was calculated to be $\frac{532nm}{2(1.3)} = 205nm$. Since

the fluorescent microspheres used to generate the PSFs are 100nm in diameter, they should be small enough to image the PSF of this fluorescence microscope. To make sure I am sampling appropriately laterally, I calculated the spot size on the sensor by multiplying the diffraction limited spot size of 205nm by the 60x magnification which resulted in a sensor spot size of $13.3\mu m$. The pixel size of $5.86\mu m$ found on the BFLY camera is less than half the size of the spot size on the sensor meaning it should be adequate to sample the PSFs laterally. The necessary axial sampling frequency(ASF) along the z-axis can be found using the equation $R_z = \frac{2(532nm)}{1.3^2} = 629nm$. An axial step size of 300nm or smaller during image acquisition therefore satisfies the Nyquist limit. To manipulate the sample axially, I used μmanager's multi-dimension image acquisition tool to control a PI microtranslation stage(M-111.1DG) with repeatability of 100nm and a resolution of 6.9nm. The rest of the system is depicted in Figure 3.2 which includes a tube lens (TL), camera, and a 532nm bandpass emission filter which can be seen as the blue square attached to the camera in Figure 3.2. This was all aligned as described in the first few steps of appendices #1.

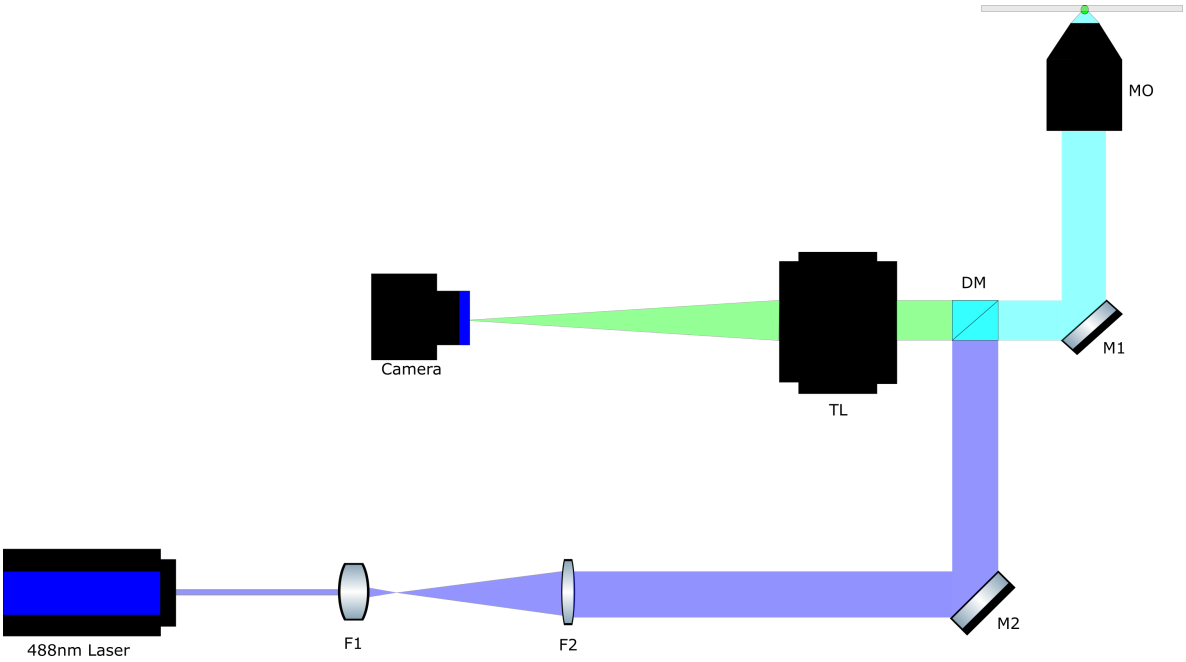

Figure 3.2: MO is an Olympus:UPlanSApo 60X/1.3 Silicone microscope objective, M1 and M2 are broadband mirrors, TL is an Olympus tube lens, DM is a 488nm highpass Semrock dichromic mirror, F2 is a biconvex 295mm lens, F1 is a 25mm biconvex lens. The 100nm yellow-green beads are imaged through a 532nm bandpass emission filter with a BFLY CMOS camera pixel size $5.86\mu m$. Image stacks were recorded by moving the stage through the focus planes.

3.2 Illumination arm redesign

One problem that I noticed early on with this first design was that focusing the illumination on the sample results in an intensity difference in the illumination as the sample moved in and out of focus. Consistent illumination through focus is important since the intensity of light emitted by the beads should be strictly due to image de-focusing and not changing illumination intensity. As a result, a re-design was made on this system to collimate light out of the objective onto the sample for a more even illumination thorough focus. To do this, I simply added a 200mm biconvex lens between mirror M2

and DM. This 200mm lens along with the Microsope objective creates an additional keplerian beam expander that will shrink the beam by a factor of $\frac{F1}{F2}$ where F1 is focal length of the microscope objective and F2 is 200mm. Since the Olympus objective has a 60X magnification and Olympus tube lenses have a focal length of 180mm, the "focal length" of the Olympus objective can be calculated as $60 = \frac{180mm}{f}$ where $f = 3mm$. With the 200mm biconvex lens, the beam diameter will be reduced from 9.44mm to $9.44mm\frac{3}{200} = 0.141mm$. With the illumination spot size on the slide should be 0.141mm and a consistent intensity regardless of the samples distance from the objective. This illumination redesign is depicted in Figure 3.3.

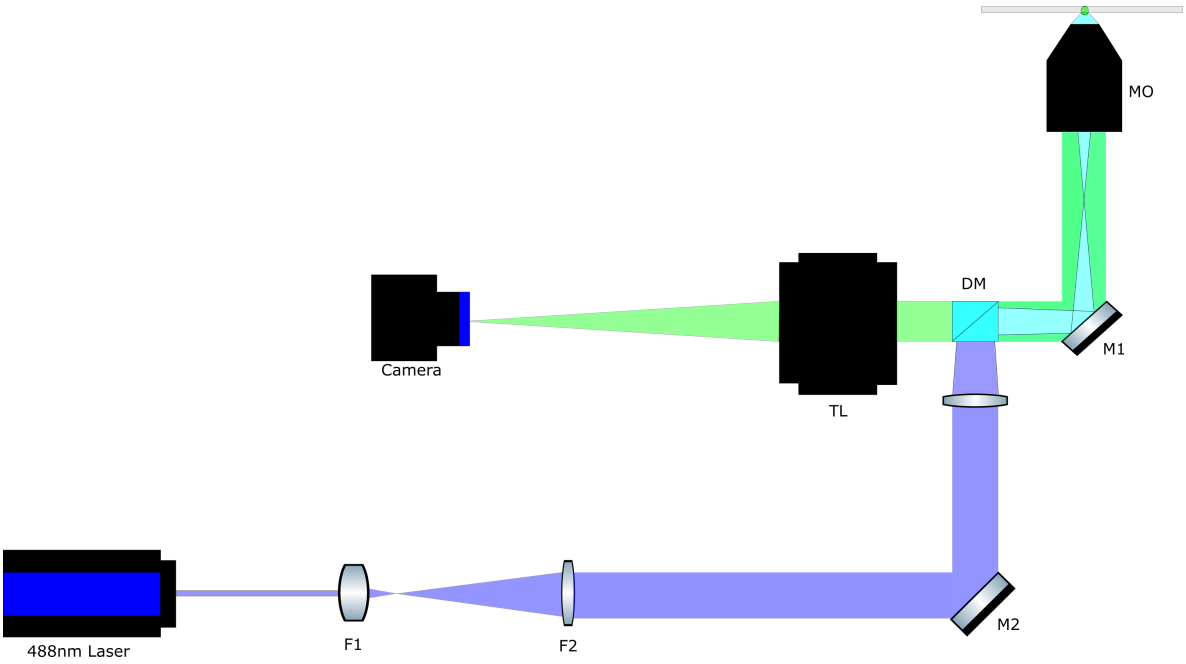

Figure 3.3: Similar to Figure 3.2, this Figure also depicts an epifluorescence microscope of the same components. However, this design is modified to have an even illumination spot size through focus via the secondary keplerian beam expander created by placing a 200mm biconvex lens between DM and M2. The illumination spot size is now 0.141mm through focus

3.2.1 Illumination Redesign Results

After the illumination redesign, I was able to record my first PSF image stacks. The leftmost image in Figure 3.4 depicts the in-focus plane's 2 dimensional PSF for what I believe to be either a small bead or a small clump of beads. This bead was selected because it was one of the most dim beads that I could find, implying it was at least a relatively small amount of beads stuck together. To find the most dim bead clumps, I plotted and checked the bead group intensity profiles to find the lowest maximum intensity value. After finding the bead that I wished to image, a multi-dimension acquisition was run by μmanager to record images at 100nm steps through the focus planes of the sample. Figures 3.4, 3.5, and 3.6 show the XY, XZ, and YZ plots of the PSF using the fire look up table (LUT) in ImageJ to emphasize the intensity differences in the pixel values. The 2D intensity profile of Figure 3.4 can be seen plotted in Figure 3.7. Figure 3.7 was used to find the optical system's resolution using the Abbe criterion by finding the distance between half maximum values and then re-scaling this to the Field of View (FOV). Using this intensity profile plot, the resolution was calculated to be around 547nm.

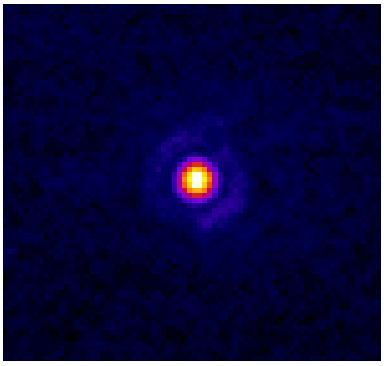

Figure 3.4: This Figure depicts the in-focus XY image of a fluorescent bead using the design in Figure 3.3. The airy disk appears to be exaggerated due to spherical aberration.

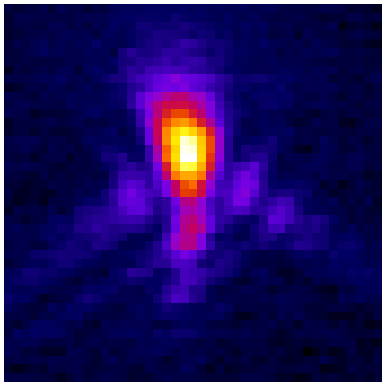

Figure 3.5: This Figure depicts the XZ orthogonal view of a fluorescent bead. The asymmetry through focus suggests a large amount of spherical aberration and it appears to look very similar to the example in Figure 2.9 from the Background section

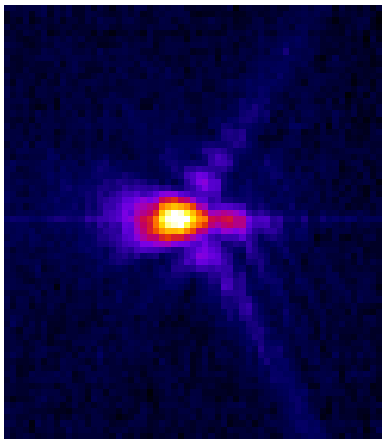

Figure 3.6: This Figure depicts the YZ orthogonal view of a fluorescent bead. The asymmetry through focus suggests, similar to Figure 3.5, a large amount of spherical aberration.

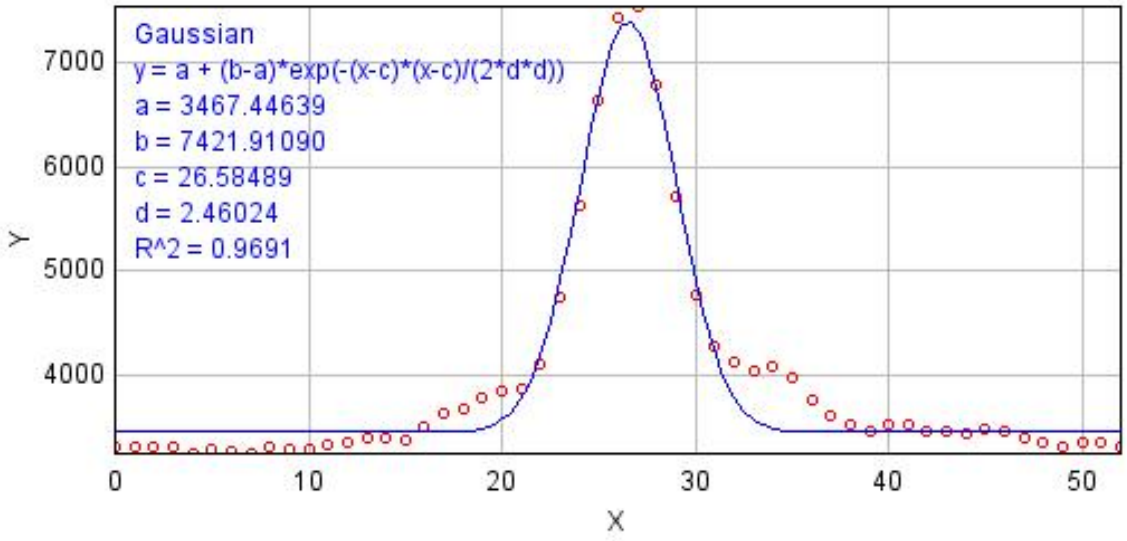

Figure 3.7: This Figure depicts a Gaussian fitting for the intensity profile of the 2D PSF from Figure 3.4. The y axis in this case is grayscale and the x axis is pixel. The experimental Abbe Resolution can be calculated from this fitting by finding the distance between the half maximum values when re-scaled to the FOV. In this case the resolution was calculated to be around 547nm.

The first thing that I noticed in the above PSF is a large amount of spherical aberration. To correct this, I first tried to adjust the correction collar on the objective until the aberrations were reduced. Objective correction collars are typically used to reduce spherical aberration in prepared slides with varying coverslip thickness. While this helped some, there was still a lot of spherical aberration in the resulting images regardless of how the collar was adjusted. I theorized that this was possibly due to poor sample preparation since the beads used to generate these images were diluted in water, deposited on the slide, and then sealed immediately. This caused for severe aberration to be present in the images as a result of refractive index mismatching between the coverslip and the water medium that the beads were suspended in. Since water's refractive index at 20 degrees Celsius is 1.33 and the silicon immersion oil's is 1.4. This would in theory result in some level of spherical aberration. To try to remedy this, I prepared more slides as described in appendix #2 of this paper where the water used to dilute the beads was evaporated in order to adhere the beads to the coverslip. Then the same immersion oil that I used for the objective was applied as a mounting medium for the beads. Now the only refractive index mismatching would be between the coverslip and possibly some immersion oil, which should be correctable using the correction collar on the microscope objective. To test this theory, I prepared a new set of slides using the immersion oil mounting medium and was able to adjust the correction collar to get rid of the spherical aberration in the images. Figures 3.8, 3.9, and 3.10 show a PSF I recorded using these new samples along xy, xz, and yz axes respectively. These Figures were cropped differently than the previous PSFs in Figures 3.4, 3.5, and 3.6, but it is apparent that this PSF is more symmetrical as the sample is moved through focus and the spherical aberration that was there previously is gone. The standard deviation value for the gaussian distribution in Figure 3.11 is lower here at 1.38 compared to the previous standard deviation of 2.46 in Figure 3.7, implying less geometric spreading in the distribution and suggesting higher resolving power. The

resolution was found to be improved from 547nm via half maximum width to 352nm with the new sample preparation, which is definitely closer to the theoretical diffraction limited Abbe resolution of 205nm calculated for this system.

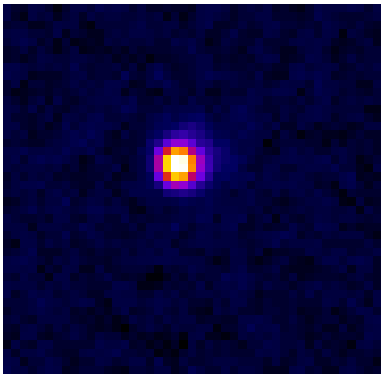

Figure 3.8: This Figure depicts the in-focus 2d image of a fluorescent bead using the design in Figure 3.3 with the new bead samples. The spherical aberration is gone but the spot appears to be very slightly smeared towards the top right corner due to some possible coma aberrations.

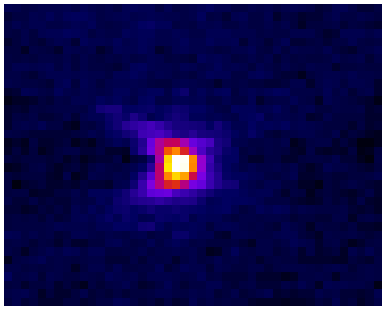

Figure 3.9: This Figure depicts the XZ orthogonal view of a fluorescent bead with the new sample preparation. While the spherical aberration is now gone, the asymmetry through focus further suggests an aberration that appears to move from the left towards the middle then out left again. This suggests coma aberration present in the system.

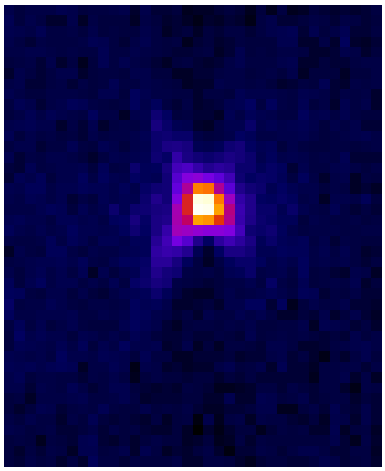

Figure 3.10: This Figure depicts the YZ orthogonal view of a fluorescent bead using the new sample preparation. This view of the PSF appears fairly symmetrical and with little aberration

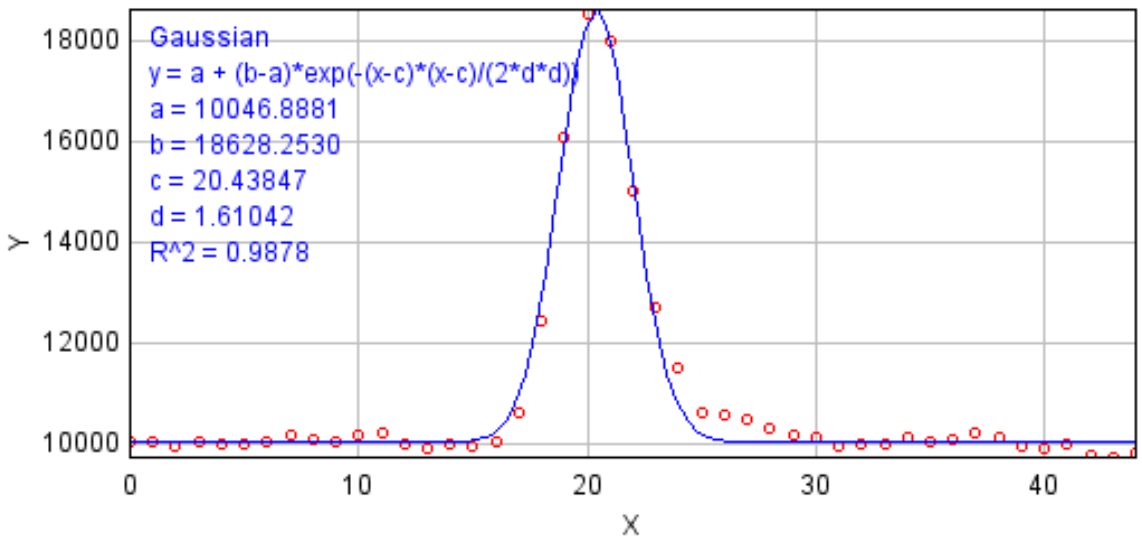

Figure 3.11: This Figure depicts a Gaussian fitting for the intensity profile of the 2D PSF from Figure 3.8. The y axis in this case is grayscale and the x axis is pixel value. The experimental Abbe Resolution was calculated by finding the full width half maximum value and when re-scaled to the FOV this was found to be 352 nm. The skewed tail is a result of the aberration present in the system

While I was happy to get rid of the spherical aberration in my PSFs via the new sample preparation technique, I realized immediately that the spherical aberration was preventing me from seeing additional aberrations entirely. The new aberrations that I saw appeared to be coma aberration. I made this conclusion based on the fact that the light from the bead appeared to move from one side and leave the same side. The bead also appeared to in focus be smeared off to one side very slightly. Coma aberration like this occurs due to some tilting misalignment in the system which results in a difference in beam path lengths. It can be difficult to locate the source of these aberrations so I tried to work backwards from the image plane by realigning the tube lens. There was no affect on the PSF so what I concluded was the aberration was being caused by either the sample not being flat with the objective or the mirror M1 not being rotated properly in its mount. I decided it would be easiest to simply realign the rotation of

mirror M1. There was no visible affect on the PSF after realignment, so I decided to test tilt the sample's orientation. To do this, I placed tape between the slide and the holder to lift the slide on one side. By this method I was able to change the direction of the aberrations that I was seeing confirming that the coma aberration was a result of sample holder misalignment.

After confirming that the aberration could be reversed by adjusting my sample holder alignment, I decided to check how flat my sample holder was with respect to the table. To do this, I used a height gauge touch probe which I borrowed from Joe Cox in the Machine shop at BSOE. I noticed that the holder's flatness with the table was dependent on its orientation when the final screws were tightened down which was causing slight misalignments. To fix this, I carefully adjusted how the sample holder was oriented until the test slide remained flat with respect to my table within a 1000th of an inch when the final screws were tightened. After taking some more PSFs, I was able to confirm that this adjustment fixed the coma aberration and I produced the PSF in Figures 3.12, 3.13, and 3.14 which depict the axes XY, XZ, and YZ respectively. The profile intensity plot at the in-focus plane is depicted in Figure 3.15. The Abbe resolution was found to be reduced to 297nm which is closer to the 205nm diffraction limited resolution than 352nm resolution that was observed before sample holder alignment. It didn't appear that there were any noticeable aberration in this PSF, so I decided that it was time to build my final lens characterization system.

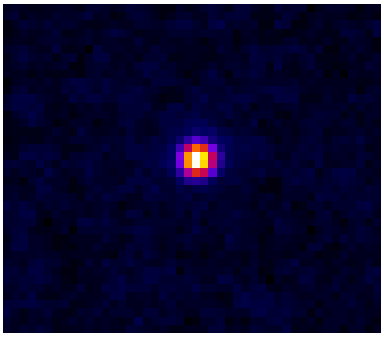

Figure 3.12: This Figure depicts the in-focus XY image of a fluorescent bead using the design in Figure 3.3 with the new bead samples and realigned sample holder. The spot appears to be more symmetrical than any of the previous PSFs from Figures 3.4 and 3.8 which showed spherical and coma aberration respectively.

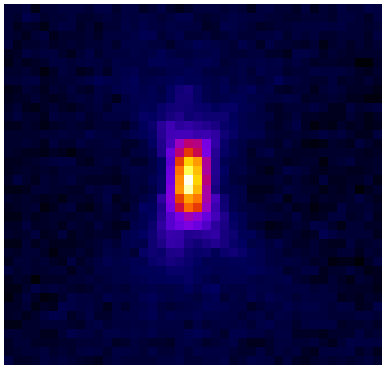

Figure 3.13: This Figure depicts the XZ orthogonal view of a fluorescent bead with the new sample preparation and realigned sample holder. This PSF appears to be fairly symmetrical axially and radially through focus.

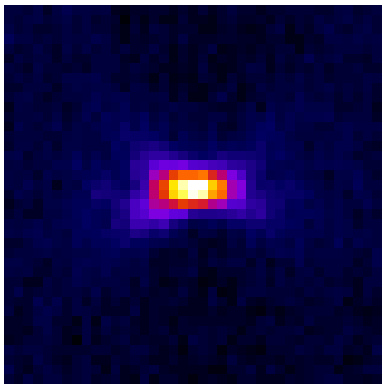

Figure 3.14: This Figure depicts the YZ orthogonal view of a fluorescent bead with the new sample preparation and realigned sample holder. This PSF appears to be fairly symmetrical axially and radially through focus.

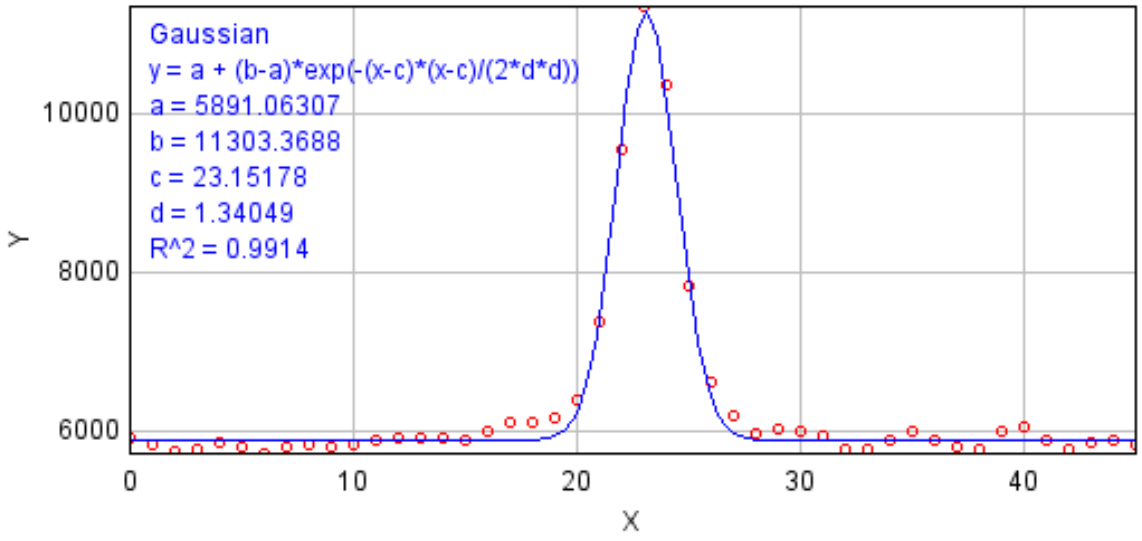

Figure 3.15: This Figure depicts a Gaussian fitting for the intensity profile of the 2D PSF from Figure 3.12. The y axis is grayscale value and the x axis is pixel value. The experimental Abbe Resolution can be calculated from this fitting by finding the distance between the half maximum values when re-scaled to the FOV. In this case the resolution is around 297nm.

3.3 Final Comparison System

After I built a fluorescence microscope and minimized its aberrations, I built the comparison system depicted in Figure 3.16. In this final design, a relay lens system is appended to the fluorescence microscope described in the previous section. To construct this relay lens system, a 150mm lens (F1) is used to collimate the image plane of the fluorescence microscope. This beam is then split into two via a 50/50 beamsplitter before the beam paths are then refocused by the two lenses(F2 and CO) on two identical but separate camera sensors. I aligned this system as described in Appendix #1 and recorded PSFs at the two secondary image planes on separate imaging channels simultaneously, using μmanager. This simultaneous imaging method allowed for me to make comparisons between the lenses with high temporal resolution. This was important for evaluating light efficiency since it is common for fluorescent samples to lose signal strength after being exposed to the laser for long periods of time. This phenomenon is called photobleaching.

For these final experiments, my advisor Sara Abrahamsson, recommended that when sampling axially, I should choose a step size for de-focus that is the re-scaled FOV pixel size. This is called the isotropic voxel and it allows for the dimensions of the PSF to be scaled equally in x, y, and z. The step size required would therefore be $\frac{5.86\mu m}{60} = 98nm$ for the microscope image plane and remains the same for the relay lens images since I am using a pair of 150mm relay lenses for F1 and CO/F2. One last small adjustment I made to this design was moving the emission filter out from the front of the camera and in between DM and TL.

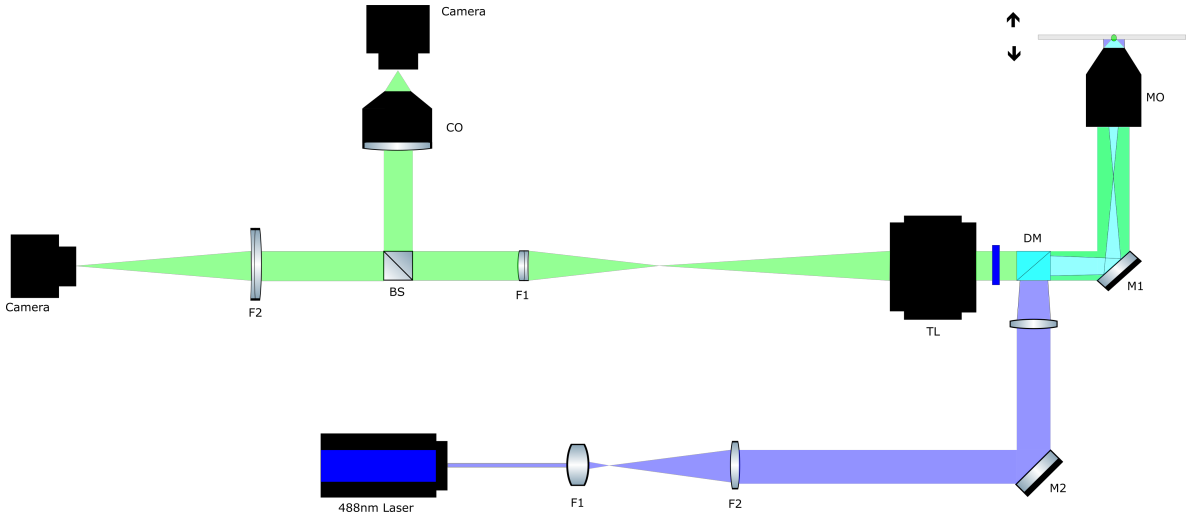

Figure 3.16: This schematic depicts my final design where a relay lens system is appended to the fluorescent microscope to reimage the primary image plane with two separate lenses. The relay lens section consists of F1(1 inch 150mm achromatic doublet), a 50/50 beamsplitter, and F2/CO to re-image the original fluorescence microscope image plane simultaneously on two identical but separate B-fly CMOS cameras. The two lenses and cameras can then be misaligned laterally by mounting them on a stage and moving them with a micrometer identical distances.

For the data in this section, I decided to use gnuplot instead of the Imagej fitting tool to fit the intensity profile plot data to Gaussian curves. This allowed for me to build functions to automatically calculate and print important values such as resolution and peak intensity. It also provided a way for me to print asymptotic error and reduced chisquare values to describe the quality of the fittings.

3.3.1 Light Efficiency Experiments

The first experiment that I wanted to do with this system was a comparison of the light efficiency of the two lenses when the system is aligned. It was expected that the many components in the camera lens would result in less light efficiency compared to the achromatic doublet. This is because light is lost via reflections off glass surfaces.

Light is also lost as it passes through the glass itself since photons excite electrons inside the glass material and are absorbed. To compare light efficiency, I took PSFs of 200nm beads prepared as outlined in Appendix #2. I chose to image 200nm beads because they require lower laser power to illuminate and are therefore less susceptible to photobleaching. I plotted the z-axis profiles from the microscope and two relay lens image planes and found the difference between background integrated density and the integrated density of the pixel values of the bead at the in-focus plane. These integrated density measurements represent the area under the surface plot curve for the 2D PSF or in other words the total light produced by the bead. I also looked at the difference between maximum and minimum pixel values in the intensity profile plot along x. What I found was 71% and 78% of the total light was seen at the achromatic doublet and camera lens image planes respectively when comparing integrated densities to the original image plane, and a 70% and 84% decrease was seen in max intensity for the achromatic doublet and camera lens respectively compared to the original image. The table below depicts these results.

	Int density	Max Intensity	Loss of light	Loss in Max intensity
Microscope	1,719,236	23038.58		
Achromatic Doublet	500,128	6938.59	71%	70%
Camera Lens	380,416	3685.91	78%	84%

After this preliminary test, I wanted to take more PSFs and fit the intensity profiles to Gaussian distributions in order to compare maximum intensities as the lenses were shifted out of alignment. Again imaging the 200nm beads, I produced the intensity profile plots in Figures 3.17 and 3.18 for camera lens and achromatic doublet respectively. Each curve corresponds to misalignment and the data was fit in gnuplot to the Gaussian distribution function

$$f(x) = Y_{min} + (Y_{max} - Y_{min})e^{(-(x-\mu)^2/(2\sigma^2)}$$

As the lens and camera moved out of alignment, both experienced a peak intensity drop. The achromatic doublet arm started in alignment at a peak of 40482 then dropped down to 36342 for the 2.5mm misalignment and finally down to 22318 for the 5mm misalignment. The camera started at a peak of 29024, then dropped to 28949 at 2.5mm, and finally to 21971 for the 5mm misalignment. The difference in peak intensity between the images produced by the two different lenses started at 11458 then dropped to 7393 at 2.5mm misalignent and finally to 347 at 5mm misalignment. This is significant because although the camera lens was less light efficient than the achromatic doublet, misalignment caused the light efficiency of the achromatic doublet to drop rapidly and approach a more similar light efficiency as the camera lens at 5mm misalignment. The geometric spreading of the image also increased with misalignment which would be expected as system resolution is likely increasing due to the misalignment. This was evident in the increased standard deviation with increased misalignment which is expressed in Figures 3.17 and 3.18 as an increase in the full width half maximum (FWHM) values reported. These values were calculated via the equation $2\sigma\sqrt{2ln(2)}$ and would represent the resolution of the system if the object being imaged were sub-resolution.

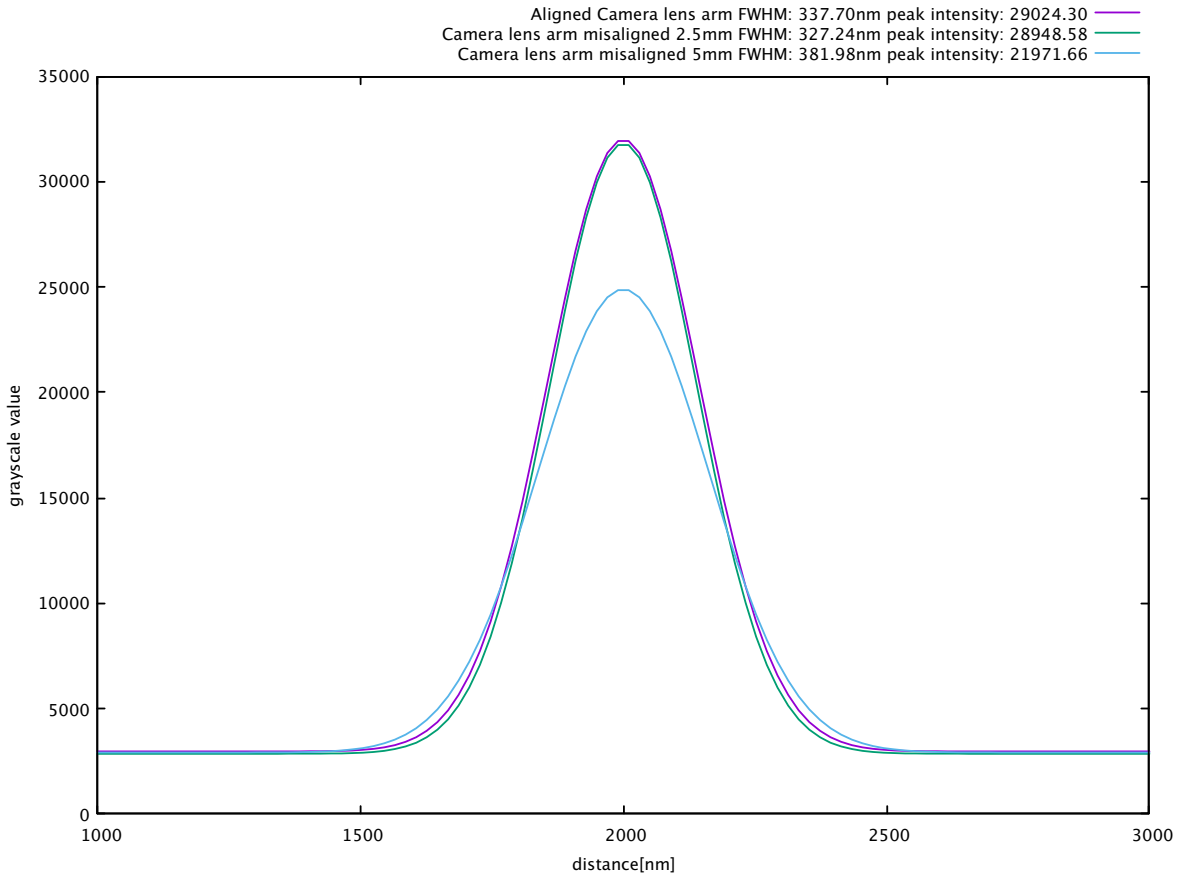

Figure 3.17: This Figure is of a Gaussian fitting to the intensity profile plot generated by imaging 200nm beads at 100ms exposure using a 0.14mW laser when the camera lens and camera were aligned, then misaligned by 2.5mm and finally misaligned by 5mm. The full width half maximum (FWHM values were found to be 338nm, 327nm, and 382nm with maximum intensity(minus noise) grayscale values of 29024, 28949, and 21972 for the aligned, 2.5mm misaligned, and 5mm misaligned positions respectively. As expected, light efficiency reduced and FWHM increased as misalignment increased. The most significant change was between the 2.5mm and 5mm misalignment where there was a sharp drop in light throughput of 24%.

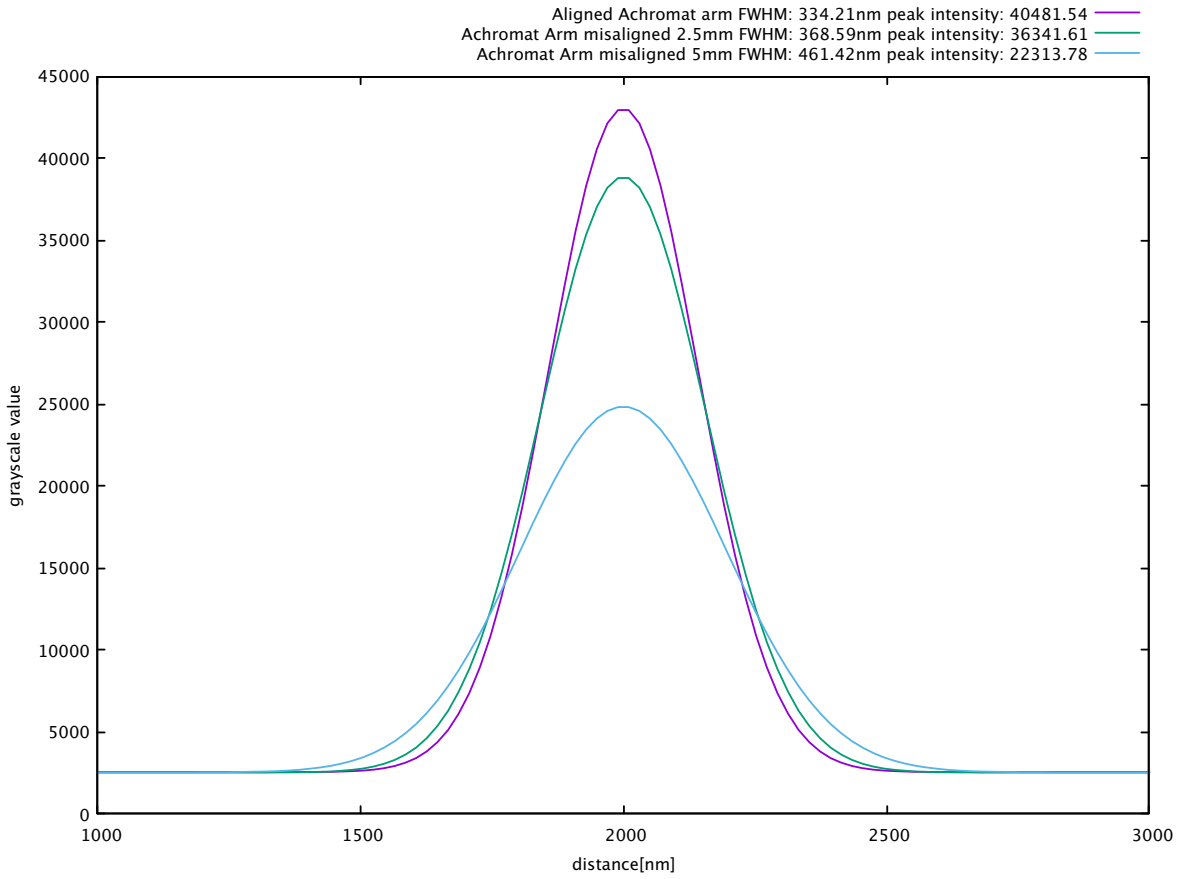

Figure 3.18: This Figure is of a Gaussian fitting to the intensity profile plot generated by imaging 200nm beads at 100ms exposure using a 0.14mW laser when the camera lens and camera were aligned, then misaligned by 2.5mm and finally misaligned by 5mm. The full width half maximum (FWHM) values were found to be 334nm, 369nm, and 461nm with maximum intensity(minus noise) grayscale values of 40482, 36342, and 22314 for the aligned, 2.5mm misaligned, and 5mm misaligned positions respectively. As expected, light throughput reduced and FWHM increased based on misalignment. Similar to the camera lens, the light throughput experienced a larger drop of 39% from 2.5mm to 5mm misalignment than 0mm to 2.5mm misalignment.

3.3.2 Resolution Experiments

Even though the data from the previous section was useful for calculating light efficiency, it was not useful for making system resolution calculations. Even though in theory the 200nm beads are smaller than 205nm theoretical resolution, the resolution calculations at the microscope image plane appeared to be over 300nm leading me to believe that this image was likely of a cluster of beads making it an object larger than the microscope objective resolution. To record PSFs to make resolution calculations, I attempted to conduct another experiment of lateral misalignment using the 100nm bead samples imaged at 500ms using a 1.7mW laser. I also tried to choose larger misalignment steps since the interesting behavior in the previous section seemed to arise at the 5mm misalignment position. I managed to produce PSFs using the two lenses at 0mm, 5mm, and 10mm misalignment as well as using the microscope plane and fit Gaussian distributions to the resulting intensity profile plots from a single bead. This fitting is depicted in Figures 3.19 and 3.20 for camera lens and achromatic doublet respectively.

For the camera lens in Figure 3.19, the microscope, aligned, 5mm misaligned, and 10mm misaligned camera arm resolutions were found to be 252 ±4.6nm, 275±9.2nm, 266±8.6nm, and 288 ±7.7nm respectively with max intensities of 6342, 2541, 2458, 2494 respectively. The relationship between resolution as a function of misalignment appeared to mostly agree with previous findings. There was a slight drop in resolution from alignment to 5mm misalignment which was strange to see until I looked at the asymptotic standard errors from fitting the data for these intensity profile plots which showed that the resolution of the aligned camera lens was 275 ±9.2 and 266 ±8.6 meaning that the resolution could have been the same or very similar and that this difference is not significant. As for the 10mm, the asymptotic standard error was also high and also in a similar range as the aligned resolution meaning resolution may or may not have had any changed significantly due to misalignment.

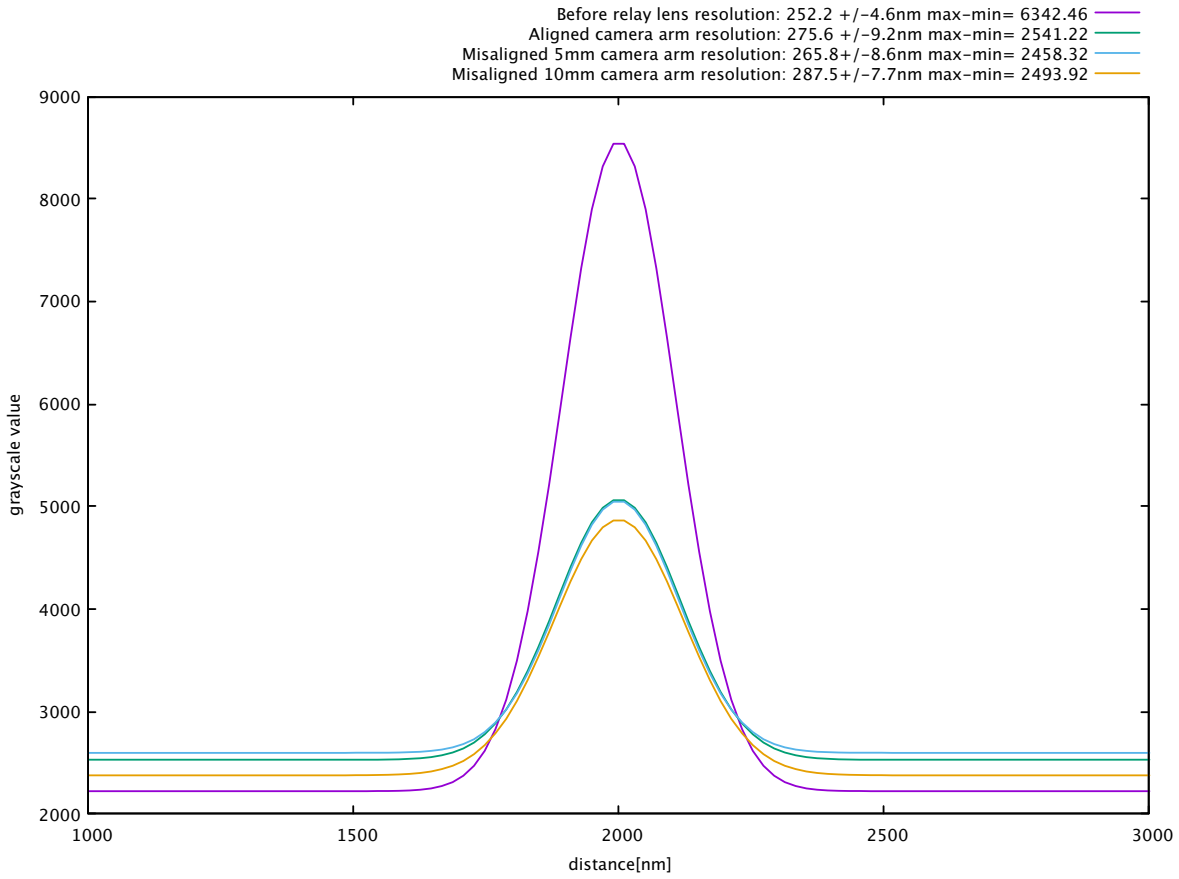

Figure 3.19: This Figure depicts Gaussian fittings for intensity profile plots of the in-focus 2D PSFs for the microscope, aligned camera arm, 5mm misaligned camera arm, and 10mm misaligned camera arm resolutions which were found to be 252±4.6nm, 275±9.2, 266±8.6nm, and 288±7.7nm with max intensities of 6342, 2541, 2458, 2494 respectively. It appeared that resolution was increasing and light efficiency was decreasing but the large asymptotic errors in fitting the standard deviations for the distributions place especially the resolution calculations in an inconclusive zone where it appears that the resolution is getting worse with misalignment, but so was the fitting.

The achromatic doublet arm data is depicted in Figure 3.20 and depicts Gaussian fittings for the microscope and aligned, misaligned 5mm, and misaligned 10mm achromatic doublet arm resolutions which were found to be 252 ±4.6nm, 280 ±9.7nm, 268 ±11.5nm, and 315 ±12.7nm respectively with max intensities of 6342, 2233, 1541, and

2347. Again, misalignment resulted in an inconclusive difference between the aligned and 5mm misalignment, however, the 10mm misaligned fitting yielded a resolution of 316±7.8nm meaning even at the worst case it would be a higher resolution than the 279.75±9.2nm resolution for the aligned system.

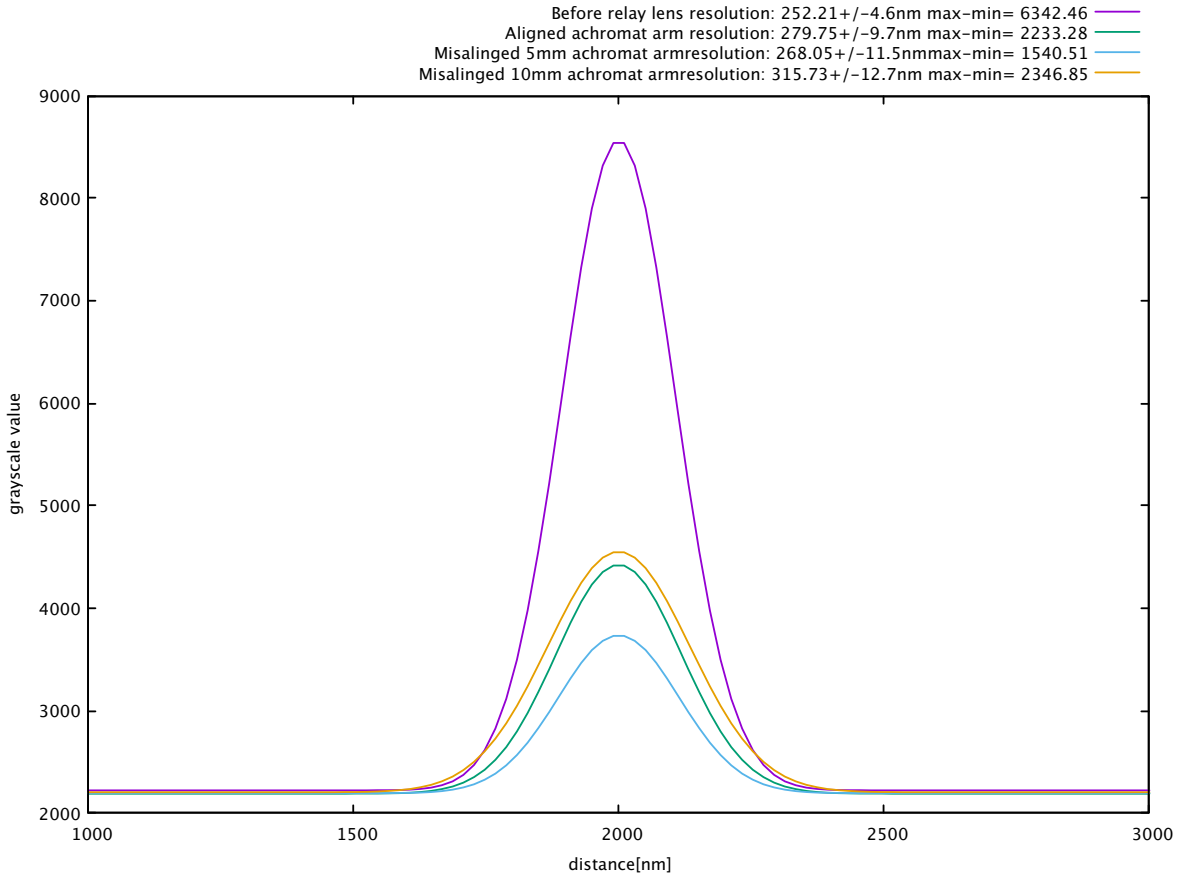

Figure 3.20: This Figure depicts the microscope, aligned achromatic doublet arm, misaligned 5mm achromatic doublet arm, and misaligned 10mm achromatic doublet arm resolutions which were found to be 252±4.6nm, 280 ±9.7nm, 268±11.5nm, and 315±12.7nm with max intensities of 6342, 2233, 1541, and 2347 respectively. There were similar fitting issues with this data as was seen in Figure 3.19, however, for the 10mm misalignment, there was a significant increase in resolution where the range for asymptotic error did not put it in the same range as for the 5mm misaligned or aligned data.

Since the 10mm achromatic doublet misalignment PSF appeared to have the worst resolution, I attempted to diagnose the aberrations by plotting the 3D PSF in Figures 3.24, 3.25, and 3.26 respectively. For comparison, I also plotted the fluorescence microscope PSF in Figures 3.21, 3.22, and 3.23 respectively. The visible differences between the two PSFs were very subtle. It almost looks like the bottom section of XZ in Figure 3.25 is a bit wider than XZ in Figure 3.22, but I am not sure if this is spherical aberration or just a noise artifact. There is a small amount of spherical aberration in the fluorescence microscope PSF which is maintained in the relayed PSF.

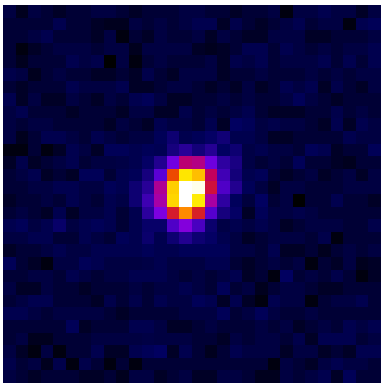

Figure 3.21: This Figure depicts the in-focus 2d image of a fluorescent bead using the fluorescence microscope. It corresponds to the before relay lens resolution intensity profile fittings in Figures 3.19 and 3.20

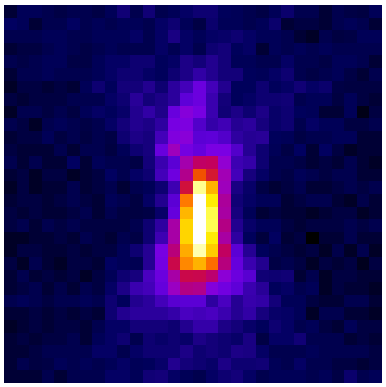

Figure 3.22: This Figure depicts the XZ orthogonal view of a fluorescent bead. This PSF was recorded using the isotropic voxel step size and appears to be fairly symmetrical axially and radially through focus with a small amount of spherical aberration.

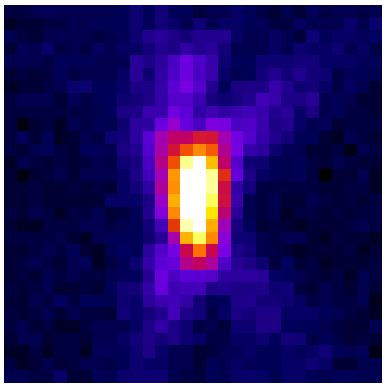

Figure 3.23: This Figure depicts the YZ orthogonal view of a fluorescent bead. This PSF was recorded using the isotropic voxel step size and appears to be fairly symmetrical axially and radially through focus with similar spherical aberration as was observed in XZ in Figure 3.22.

After conducting this experiment, I noticed some strange things going on with the light output from the 100nm beads. They appeared to photobleach quickly under the high laser power required to image them with a reasonable STNR. This was typically over 1mW laser power for 500ms exposures for image stacks that were at least 50 images to ensure the whole PSF was taken. That means the beads were exposed to the 1mW

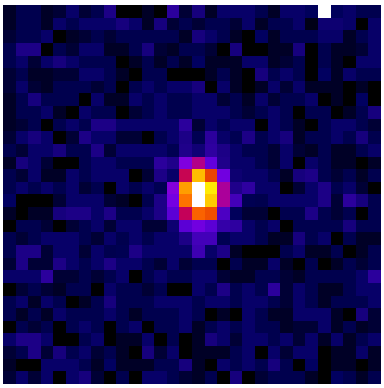

Figure 3.24: This Figure depicts the in-focus 2d image of a fluorescent bead using 10mm misaligned achromatic doublet arm. The intensity profile fitting can be found in Figure 3.20.

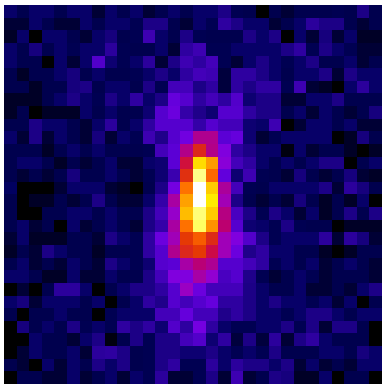

Figure 3.25: This Figure depicts the XZ orthogonal view of a fluorescent bead imaged with the 10mm achromatic doublet arm using the isotropic voxel sampling. This PSF appears to be fairly symmetrical axially and radially through focus with a small amount of spherical aberration.

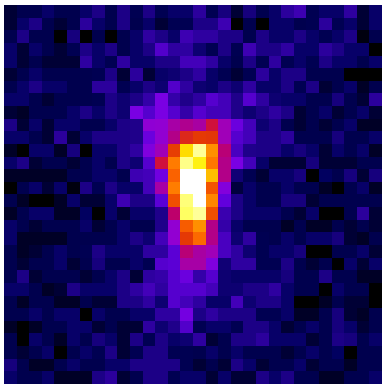

Figure 3.26: This Figure depicts the YZ orthogonal view of a fluorescent bead imaged using the 10mm misaligned achromatic doublet arm using the isotropic voxel sampling. This PSF appears to be fairly symmetrical axially and radially through focus with similar spherical aberration as was observed in XZ in Figure 3.22.

laser for a total of 25 seconds per PSF recording. Therefore, I wanted to see if, after the many imaging cycles, this might have an effect on the PSFs. To test this, I recorded the response of the 100nm beads over a 5 minute period at 500ms exposures every 5 seconds with a laser power of 1.7mW. The integrated densities were then fit to a line and a quadratic equation as depicted in Figure 3.27. I did the same with the max intensity data from this imaging sequence and fit it in Figure 3.28. This data was relatively noisy but it is apparent that there is a noticeable decrease in fluorescence that happens in especially the first 100 seconds of exposure. With the long exposures required to take PSFs of the 100nm beads, it is likely that the light efficiency data would be affected by this reduction in signal with respect to illumination time.

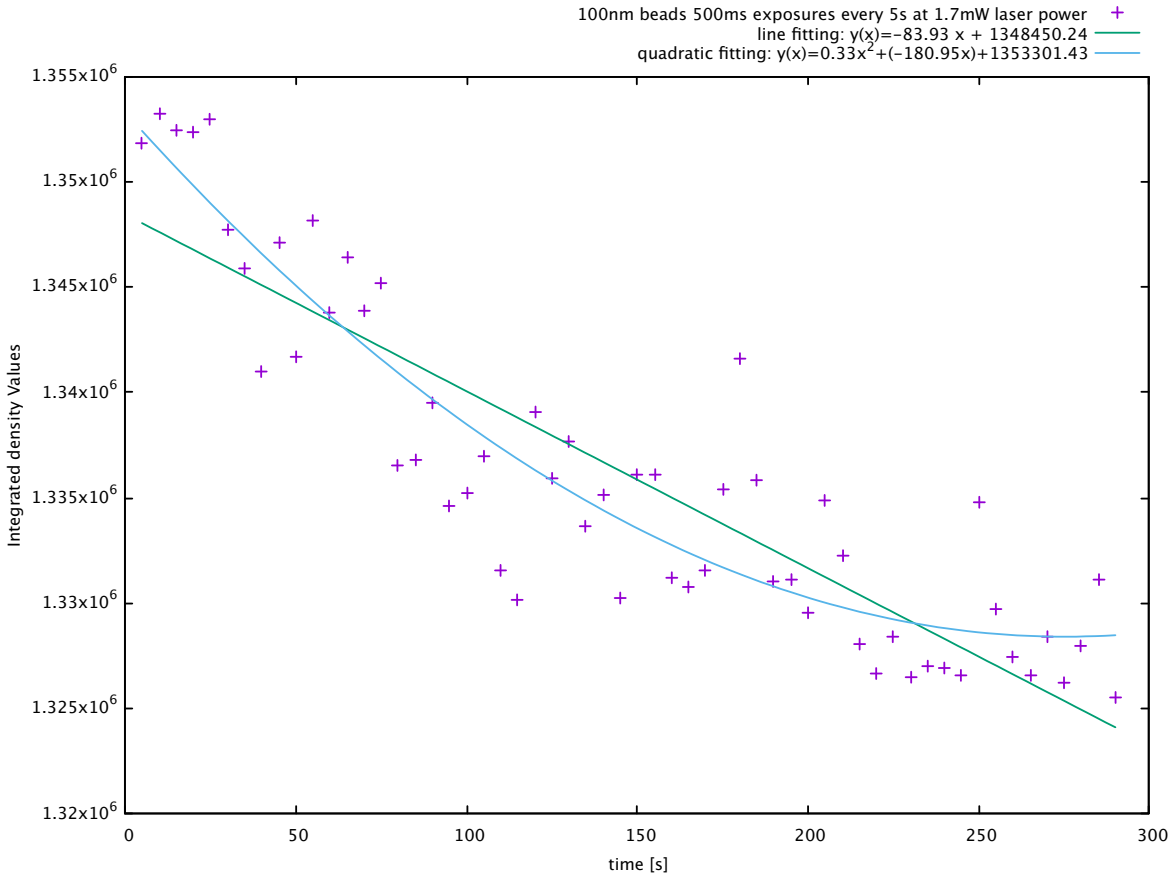

Figure 3.27: This Figure depicts some 100nm bead data that I recorded with 500ms exposures at 5s intervals with a 1.7mW illumination. This is the same laser power and exposure that was used for the 100nm bead data in the intensity profile plots depicted in Figures 3.19 and 3.20. After fitting a line and quadratic equation to the data, the reduced chisquare was found to be 1.464e7 for the line and 1.043e7 for the quadratic implying the quadratic fit better but neither fit very well likely due to noise. I am not sure if this Figure is sufficient for modeling the behavior of these beads, but it is apparent that photobleaching in these beads is definitely an issue when conducting light efficiency experiments since typically with the 100nm beads high laser power is required to illuminate them.

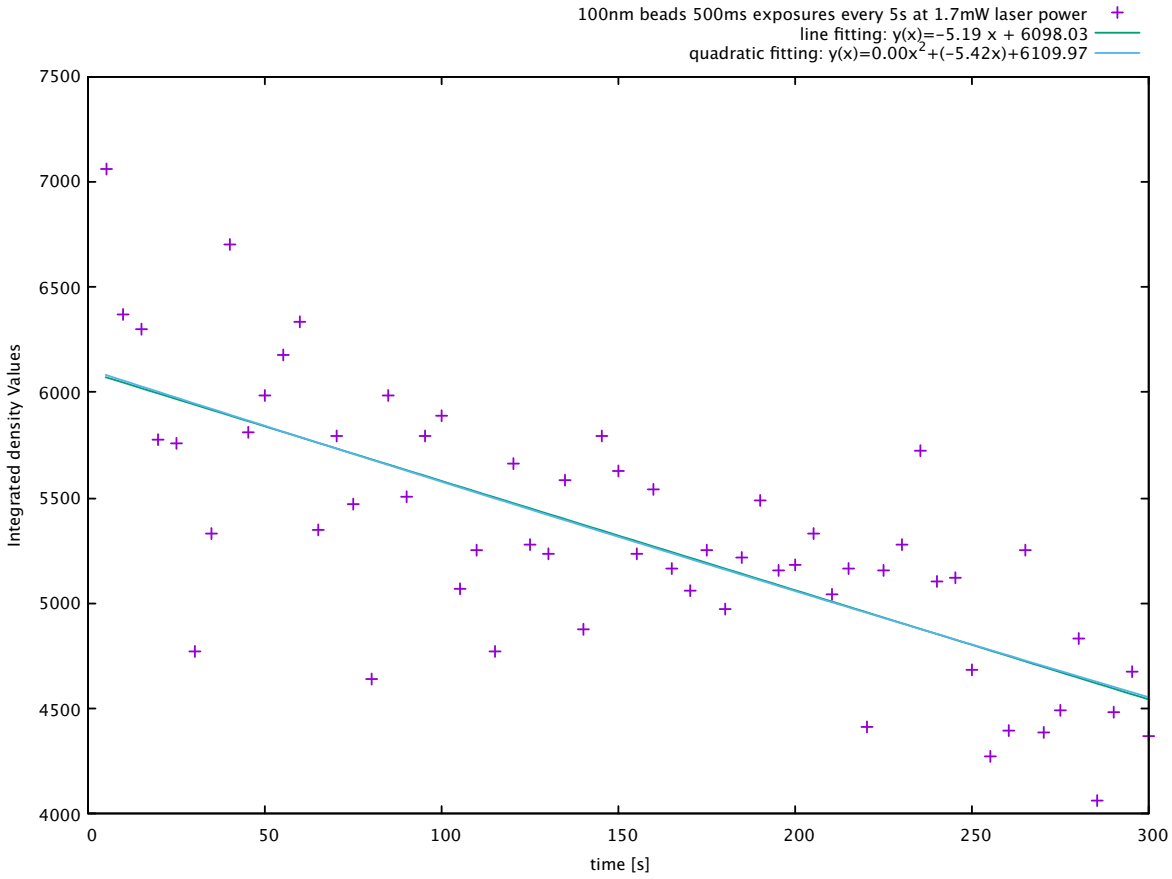

Figure 3.28: This Figure depicts the maximum intensity measued for the 100nm bead data that I recorded with 500ms exposures at 5s intervals with a 1.7mW illumination. There is an obvious decrease in fluorescence maximum intensity as a function of time here but it appears to be more linear. I tried again to fit the data to a line and quadratic formula but it seemed to be more linear in this case. This is a large drop in maximum grayscale value and would definitely affect some of the later PSFs taken in the previous section for the 100nm bead data.

4 Conclusion

After building a fluorescence microscope that displayed minimal aberrations when imaging my prepared bead samples, I successfully built a lens characterization system to compare the light efficiency and aberration robustness of the camera lens to the achromatic doublet lens. In the process, I wrote protocols for both aligning my lens characterization system as well as preparing fluorescent bead samples. Lastly, I attempted to characterized the signal loss in the 100nm fluorescent beads as a function of time exposed to an illumination laser.

After conducting my first few experiments to determine the light efficiency of the two lenses, I noticed that although the achromatic doublet lens was more light efficient than the camera lens when the system was aligned, the light efficiency of the two lenses appeared to approach each other as the system was misaligned laterally by an amount of 10mm. This is interesting because it implies that when it comes to light throughput, the outer regions of the camera lens are more consistent with the center region than the achromatic doublet's outer regions are with its center region. This may be an important quality to this secondary relay lens for MFM systems since it is important that the outer regions of the glass are focusing the different diffraction orders with similar light efficiency. Therefore, it is possible that using the camera lens is more effective than the achromatic doublet for MFM applications where uniform intensity in the diffraction orders of light is desired.

While I didn't seem to have many issues with fitting errors for the minimum and

maximum in the plots for the light efficiency calculations using the 200mm beads, my methods did seem to have issues with carefully quantifying standard deviation and system resolution calculations when the resolutions were very close for the 100nm bead PSFs. I think this was due to the increase in noise when imaging the 100nm beads as opposed to the 200nm beads and also sampling laterally at a resolution that was very close to the PSF spot size. This yielded only a few pixels for collecting the PSF data for intensity profile plots and could have lead to the uncertainty in the standard deviation parameter resulting from the fittings. As for the recorded resolution comparisons, it appeared that the only conclusive resolution change was for the achromatic doublet when it was misalignment by 10mm. I could not identify specifically what aberration was causing the worse resolution, but there is evidence that some is present. Again these findings suggest that the outer regions of the camera lens may outperform the outer regions of the achromatic doublet, but further experimentation should be done to confirm this.

5 Future Work

For future work, the first thing I would do to generate better PSF data is increase the lateral sampling frequency by increasing the magnification. I would also take many PSFs and average them in an attempt to reduce noise. I think these two things would help generate intensity profiles that would be easier to fit to the Gaussian distributions and would yield better resolution calculations, but unfortunately I ran out of time to try these two things.

The next thing that I would do is generate better fluorescent bead signal deterioration models. After realizing how susceptible the fluorescent beads are to photobleaching, I now realize how important it is to model this signal loss especially when conducting long exposures with the 100nm beads. If I had more time with this project, I would definitely conduct more extensive experiments to come up with models for the deterioration of the bead signal.

Another thing I would want to try is increasing the misalignment of the lenses to the 20mm misalignment range or even up to the 50mm misalignment range. I think this would be interesting because the reported data leads me to believe there would be a much larger difference in both resolution and light efficiency when comparing the two lenses.

Beyond lens characterization, an interesting avenue for future work with this system would be to use it to characterize other optics, fluorescent samples, and cameras. For example, I have managed to use this system to do signal to noise ratio and gain exper-

iments to compare the Andor Xion888 EMCCD to the Prime 95B backlit EMCCD.

Finally, I would like to design some alignment tools to ease in the alignment procedure. For example, an objective mount similar to the Halo alignment tool could be constructed in order to launch a wide collimated beam into the system. This would aid in finding the focal planes of the system. Also, a tool that launches a flat grid of straight beams, possible a 3x3 array, might aid in aligning the rotation of the mirror M1 under the objective holder.

6 Appendix #1: Alignment

In this section, I will describe step by step the alignment procedure that I use for this comparison system. Much of the procedure described in this section is based on the procedures found in the appendices of a paper by Sara Abrahamsson et al. (2015) describing the alignment for a multifocus microscope [2].

6.1 Microscope Materials

- 100nm yellow-green fluorescent microsphere slides (see Appendix 2)
- PI microtranslation stage(M-111.1DG)
- PI C-863.11 controller
- Olympus:UPlanSApo 60X/1.30 Sil microscope objective
- 2 1 inch Broadband dielectric mirrors 350-700nm
- Semrock 488nm Dichromic mirror (Di03-R488-t3-25x36)
- 180mm Olympus Tube lens U-TLU (infinity corrected)
- 2 inch 150mm Acromatic Doublet
- Newport Non-pol cube beamsplitter 400-700nm
- 2 inch Broadband dielectric mirror 350-700mm

- Olympus Zuiko Digital ED 150mm f/2 Camera Lens
- Edmund optics 3inch diameter 150mm acromatic doublet lens
- Semrock 532nm bandpass emission filter (FF01-532/3-25)
- 2 FLIR BFLY-U3-23S6M-C CMOS camera
- spectra-physics 20mW Cyan Laser (488nm)
- Variable ND Filter (0-2.5)
- 1 inch diameter 25mm BiConvex lens
- 1 inch diameter 295mm BiConvex lens
- 1 inch diameter 200mm BiConvex lens

6.2 Alignment Materials

- 2 Iris Apertures
- Target with crosshairs
- Thorlabs green collimated laser diode (532nm)
- Halo housed red laser
- Thick card stock with pinhole
- Shear Plate
- Dry erase marker

6.3 Procedure

- The first step to aligning this system is aligning the Halo. If the Halo is well aligned, the assumption is that the Halo's beam will be orthogonal to the table when screwed into the objective holder. This allows for the rest of the system to be aligned based on this initial beam, meaning aligning the Halo is an extremely important first step to system alignment. The Halo alignment procedure is outlined in Sara Abrahamsson et al. (2015) [2].

- Another important early step in aligning an optical system of this type is making a decision on system beam height. Usually this decision will be made based on the tallest or least flexible component in the design. In this case, this is the breadboard/stage portion in which the cameras, and second relay lenses are mounted. I determined at this stage the beam height of my final design to be roughly 5 inches above the table surface.

- After establishing an approximate beam height, I begin aligning the beam routes. I start by adjusting the rotation of mirror M1 in its mount. This alignment is important because if M1 is sitting rotated off axis, the beam paths will be slightly different lengths for the light that is leaving the objective and hitting opposite sides of this mirror, resulting in aberrations. To ensure the rotation of M1 is aligned, I screw the Halo into the objective holder and then aim the beam across the table. I will then tilt the mirror in the mount to move the beam up and down. If the beam is moving off axis unexpectedly, it should be rotated in the mount until it is moving only the direction you intended to move it. After adjusting the rotation of this mirror, I set the center of the mirror to be at the approximate system beam height determined in the previous step.

- Next, I will align mirror M1 such that the halo beam is being reflected parallel to

the table and is traveling the path directly over a row of selected table holes. This should be done by setting two apertures at the desired height close to the objective and then positioning one far away. Walk the beam into alignment as outlined in an optomechanical alignment paper by Phil Scott [**?**]. It should be noted that the position of the beam at the first aperture should be adjusted by moving the objective holder and the position of the beam hitting the second aperture should be adjusted by changing the angle of mirror M1. I have found it helpful to use a collar to ensure the height of these apertures does not change in future alignment steps since this step dictates final system beam height. At this step, I will also mark the emission beam path on the table with an arrow.

- After aligning M1, I will begin aligning the illumination beam path for the system using dichroic mirror (DM) and mirror M2. By placing DM in the beam path, the halo beam can be seen reflecting off the surface of the glass. I use this reflection off the front surface to align the dichroic mirror to reflect the beam over a set of table holes using the two apertures at their set height to walk the beam. Keep in mind that the halo should also be hitting DM close to the center so as to not crop the image. When choosing the position of DM also keep in mind that the distance between TL and objective is relatively small (at approx 180mm) meaning that the dichroic mirror needs to be positioned relatively close to M1 to leave enough room for TL. After aligning DM, I will then reflect the beam with M2 along a set of table holes using the two apertures to walk the beam.

- Next, I position the 488nm laser in the beam path so that it is reflecting off M2, DM, and M1. It is useful to significantly reduce the power of the illumination laser at this stage using either software or an ND filter. Using an aperture close to the laser and one between DM and M1, I will then walk the illumination beam into alignment with the Halo beam path. Optical tissue can be useful for checking the beam paths to ensure the halo and illumination laser are the on the same

path. Now, both beams should be hitting M1 at the same point in the center of the mirror and the beam paths between M1 and DM should be the same for illumination and emission.

- After establishing the beam paths for illumination and emission, the illumination beam can be modified. For this design, I used two keplarian beam expanders to launch a collimated beam out of the objective and onto the sample. To do this, I use a 25mm biconvex lens with a 250mm biconvex lens to expand and collimate the beam between illumination laser and mirror M2. The distance between the lenses should be the sum of the two lens focal lengths, which in this case is 275mm. To find this exact distance, I launch the beam through the two lenses and onto a shear plate. I then adjust the distance between the lenses until the appropriate distance to collimate the beam has been found. I mark this position on the table and then align the two lenses using the back-reflections and a target or aperture as outlined in [2]. It can also be useful to take a picture of where the aligned illumination laser is hitting on the ceiling and use that to as a target to align the illumination lenses[1]

- Finally, I position the 200mm biconvex lens between DM and M2. I find the distance between this lens and the objective by moving the lens along the illumination axis until the beam launching from the objective appears to be collimated. This will be evident when the beam is not diverging or converging anymore and it will appear to be focused on the ceiling. The assumption here is that the distance between the objective and the ceiling is infinite with respect to the objective working distance and the beam appears focused because the rays propagating out of the objective are collimated. After this distance is found, I mark the table and proceed to align the lens using the target and back reflections.

[1]Shear plates are interferometers that allow the user to make inferences about the angle of the rays that enter it by producing two reflections of the entering beam to visibly show the interference patterns between the rays.

- At this point, the illumination arm of the system is aligned. To begin aligning the emission arm of the system, the distance between microscope objective (MO) and the tube lens (TL) should be found. To do this, I shoot a collimated laser through TL and MO and adjust the position of TL in an attempt to collimate the beam out of the objective on the ceiling as was done for the lens between DM and M2. After this distance is found, I mark the position for TL on the table and proceed to screw the halo into the objective holder.

- Now it should be noted that the beam path for the halo has shifted after passing through the dichroic mirror. A target should be placed at the end of the table such that the halo is hitting it in the center when passing through DM alone. Now align TL using the pinhole and target.

- If properly aligned, at this stage a fluorescence microscope has been built. I will then position a camera behind TL and find precise camera position by shooting the collimated beam into the objective holder and adjusting the camera's distance from TL until the laser appears to be focused on the camera sensor. After this distance is found, I will then align the camera by imaging the halo and using a pinhole to align back reflections off the sensor. I have found it useful to remove this camera but leave the aligned mount so that this image plane can be quickly switched back to later.

- A similar procedure to finding the distance between TL and MO can be done to place the first relay lens F1 along the optical axis. Remove the objective and launch the collimated beam through the first relay lens F1 and the tube lens TL. Adjust the position on the optical axis of relay lens F1 such that the light is focused on the ceiling. Mark the focused position on the table and align this lens using the Halo, target, and pinhole.

- Next, Position the 50/50 beamsplitter (BS) in the beam path. Align the reflection

off the front surface with a pinhole. 50% of the halo is now being reflected perpendicular to the beampath. Place an additional target so the reflected beam is now hitting the center of this target. This will be used to align CO in the next step.

- I then screw in the objective MO and find the correct position along the optical axis for lenses F2 and CO using the collimated laser as done in previous steps by focusing the beam on the ceiling. Again, I will mark the table as was done for F1 and TL and align these final two lenses again with the Halo, target, and pinhole.

- Next, I will find the position along the optical axis for camera placement behind F1 and TL. This step can be tricky as it is sometimes difficult to determine exactly what distance something appears to be in focus. What I have decided is best is to focus the camera lens using the olympus camera body at infinity. This produces a precise image plane on the olympus camera sensor which I use to focus some beads by adjusting their position with respect to the objective. I will then remove the olympus camera and position both cameras behind F1 and TL such that they are in focus without moving the sample. After finding the appropriate camera distances and marking these locations on the table, I align the cameras with the halo and pinhole again to ensure the beam is centered on the camera sensors and the beam is being reflected back through the pinhole. Alternatively, you can position the camera in the fluorescence microscope image plane to focus the sample and then switch the camera back out to the secondary relay lens and adjust its position until it is in focus.

- Finally, position the emission filter between DM and TL. Use the halo to align the back reflection off the filter and try to position the filter so that the halo is hitting it in the center.

7 Appendix #2: Sample Preparation

7.1 Materials

- Fluospheres kit 2 Carboxylate-modified Microspheres yellow-green 100nm and 200nm
- Fisherbrand Microscope Cover Glass 12-541A 18X18-1.5
- Fisherbrand Superfrost plus Microscope Slides 12-550-15 25x75x1 mm
- Vortexer
- Olympus silicone immersion oil
- Nail Polish Hardener
- Eppendorf Micropipettes 20-200l, 2-25l

The fluorescent beads that serve as point sources for my PSF measurements are FluoSphere Carboxylate-modified Microspheres yellow-green which arrived suspended in solution at a 2% solid concentration. The main concerns for me during sample preparation were reducing aggregation in the solution and ensuring that the beads were diluted enough as to not interfere with each other during PSF acquisition. To do

this, the beads were vortexed and then diluted in de-ionized water at factors of 1:100. A large dilution of $1 : 10^6$ or more produces sufficiently spread fields of beads any more and it can be difficult to sometimes be difficult to locate the field of beads. Then, $15mu$l of the diluted bead solution was deposited on a cover slip and left to dry overnight. This ensured that the beads would adhere to the coverslip, which is important since imaging through thick layers of mounting medium can induce spherical aberration. The next day, I placed 12l of silicone oil on the slide and then dropped the coverslip onto the slide at a 45 degree angle. I then pressed down on the coverslip lightly to ensure the deposition of a thin layer of immersion oil and push the air bubbles out of the medium. This also helps to flatten the coverslip against the slide which can solve issues with coverslip misalignment which can be an issue since the medium used here is relatively viscous. Finally, the coverslips were sealed with clear nail polish hardener and left to dry. A far more rigorous sample prep outline can be found in a paper by Richard W Cole et al. (2011) which is what I based this preparation outline on[11]. However in my experience a large dilution like the one described resulted in fields of beads that were sparse and minimally aggregated allowing for PSFs to be recorded.

Bibliography

[1] Sara Abrahamsson, Jiji Chen, Bassam Hajj, Sjoerd Stallinga, Alexander Y Katsov, Jan Wisniewski, Gaku Mizuguchi, Pierre Soule, Florian Mueller, Claire Dugast Darzacq, Xavier Darzacq, Carl Wu, Cornelia I Bargmann, David A Agard, Maxime Dahan, and Mats G L Gustafsson. Fast multicolor 3D imaging using aberration-corrected multifocus microscopy . *Nature Methods*, 10:60 EP, 2012.

[2] Sara Abrahamsson, Molly McQuilken, Shalin B. Mehta, Amitabh Verma, Johannes Larsch, Rob Ilic, Rainer Heintzmann, Cornelia I. Bargmann, Amy S. Gladfelter, and Rudolf Oldenbourg. Multifocus polarization microscope (mf- polscope) for 3d polarization imaging of up to 25 focal planes simultaneously. *Opt. Express*, 23.

[3] D. A. Agard J. W. Sedat B. M. Hanser, M. G. L. Gustafsson. Phase-retrieved pupil functions in wide-field fluorescence microscopy . *Journal of Microscopy*, 216:32–48, 2004.

[4] J Enoch. First known lenses originating in Egypt about 4600 years ago! . *Hindsight*, 31(2):9–17, 2000.

[5] Werner Göbel, Björn M Kampa, and Fritjof Helmchen. Imaging cellular network dynamics in three dimensions using fast 3D laser scanning . *Nature Methods*, 4(9):73, 2006.

[6] D. Van Ras I. Gris-Sánchez and T. A. Birks. The Airy fiber: an optical fiber that guides light diffracted by a circular aperture . *Optica*, 3:270–276, 2016.

[7] Nicolas Passilly Luc Froehly Jorge Albero Sylwester Bargiel Maciej Baranski, Stephane Perrin and Christophe Gorecki. A simple method for quality evaluation of micro-optical components based on 3D IPSF measurement . *Optics Express*, 22:13202–13212, 2014.

[8] David Mendlovic and Haldun M. Ozaktas. Fractional Fourier transforms and their optical implementation: I . *Journal of the Optical Society of America A*, 10(9):1875–1881, 1993.

[9] Haldun M. Ozaktas. Fractional Fourier transforms and their optical implementation: I . *2001 European Control Conference (ECC)*, 2001.

[10] Peter J. Shaw David J. Rawlins. The point-spread function of a confocal microscope: its measurement and use in deconvolution of 3-D data . *Journal of Microscopy*, 163(2):151–165, 1991.

[11] Claire M Brown Agard Richard W Cole, Tushare Jinadasa. Measuring and interpreting point spread functions to determine confocal microscope resolution and ensure quality . *Nature Protocols*, 6(12):1929–41, 2011.

[12] Ernst H. K. Stelzer. Beyond the diffraction limit? . *Nature*, 417:806–807, 2002.